ANALYSIS OF CYLINDRICAL REFLECTOR ANTENNAS IN THE PRESENCE OF CIRCULAR RADOMES BY COMPLEX SOURCE – DUAL SERIES APPROACH

A DISSERTATION

SUBMITTED TO THE DEPARTMENT OF ELECTRICAL AND ELECTRONICS ENGINEERING

AND THE INSTITUTE OF ENGINEERING AND SCIENCES OF BILKENT UNIVERSITY IN PARTIAL FULFILLMENT OF THE REQUIREMENTS

FOR THE DEGREE OF DOCTOR OF PHILOSOPHY

By

Taner Oğuzer

November 1996

ANALYSIS OF CYLINDRICAL REFLECTOR ANTENNAS IN THE PRESENCE OF CIRCULAR RADOMES BY COMPLEX SOURCE-DUAL SERIES APPROACH

A DISSERTATION

SUBMITTED TO THE DEPARTMENT OF ELECTRICAL AND

ELECTRONICS ENGINEERING

AND THE INSTITUTE OF ENGINEERING AND SCIENCES

OF BILKENT UNIVERSITY

IN PARTIAL FULFILLMENT OF THE REQUIREMENTS

FOR THE DEGREE OF

DOCTOR OF PHILOSOPHY

By

Taner Oğuzer

November 1996

I certify that I have read this thesis and that in my opinion it is fully adequate, in scope and in quality, as a dissertation for the degree of Doctor of Philosophy.

Prof. Dr. Ayhan Altıntaş(Supervisor)

I certify that I have read this thesis and that in my opinion it is fully adequate, in scope and in quality, as a dissertation for the degree of Doctor of Philosophy.

Assoc. Prof. Dr. İrşadi Aksun

I certify that I have read this thesis and that in my opinion it is fully adequate, in scope and in quality, as a dissertation for the degree of Doctor of Philosophy.

Dr. Vladimir Yurchenko

I certify that I have read this thesis and that in my opinion it is fully adequate, in scope and in quality, as a dissertation for the degree of Doctor of Philosophy.

Assoc. Prof. Dr. Uğurhan Muğan

I certify that I have read this thesis and that in my opinion it is fully adequate, in scope and in quality, as a dissertation for the degree of Doctor of Philosophy.

Assoc. Prof. Dr. Gülbin Dural

Approved for the Institute of Engineering and Sciences:

Prof. Dr. Mehmet Baray
Director of Institute of Engineering and Sciences

ABSTRACT

ANALYSIS OF CYLINDRICAL REFLECTOR ANTENNAS IN THE PRESENCE OF CIRCULAR RADOMES BY COMPLEX SOURCE-DUAL SERIES APPROACH

Taner Oğuzer
Ph. D. in Electrical and Electronics Engineering
Supervisor: Prof. Dr. Ayhan Altıntaş
November 1996

The radiation from cylindrical reflector antennas is analyzed in an accurate manner for both H and E polarization cases. The problem is first formulated in terms of the dual series equations and then it is regularized by the Riemann-Hilbert Problem technique. The resulting matrix equation is solved numerically with a guaranteed accuracy, and remarkably little CPU time is needed. The feed directivity is included in the analysis by the complex source point method. Various characteristic patterns are obtained for the front and offset-fed reflector antenna geometries with this analysis and some comparisons are made with the high frequency techniques. The directivity and radiated power properties are also studied. Furthermore, the results are also compared by the Method Of Moments and Physical Optics solutions. Then the case of circular radome enclosing the reflector is considered. Radomes concentric with the reflector are examined first, followed by the non-concentric radomes.

Keywords: Cylindrical reflector antennas, Radiation, Radome, Dual series equations.

ÖZET

DAİRESEL RADOMLU SİLİNDİRİK YANSITICI ANTENLERİN KARMAŞIK KAYNAK-İKİLİ SERİLER YAKLAŞIMIYLA ANALİZİ

Taner Oğuzer
Elektrik ve Elektronik Mühendisliği Bölümü Doktora
Tez Yöneticisi: Prof. Dr. Ayhan Altıntaş
Kasım 1996

Silindirik yansıtıcı antenlerden radyasyon her iki H and E polarizasyonlar için hassas bir biçimde analiz edildi. Problem önce ikili seri denklemleriyle formüle edildi ve sonra Riemann-Hilbert tekniğiyle düzenlileştirildi. Sonuçtaki matris denklemi nümerik olarak garantili hassasiyetle çözüldü. Kaynak kazancı analize karmaşık kaynak noktası yöntemiyle dahil edildi. Pek çok karakteristik örnekler önden ve kaydırılmış beslemeli yansıtıcı anten geometrileri için aynı yöntemle elde edildi ve yüksek frekans teknikleriyle bazı karşılaştırmalar yapıldı. Kazanç ve radyasyon gücü özellikleri üzerinde de çalışıldı. Ayrıca, sonuçlar moment yöntemi ve fiziksel optik çözümleriylede karşılaştırıldı. Daha sonra yansıtıcıyı çevreleyen dairesel radom durumu düşünüldü. Yansıtıcı ile ortak merkezli radomlar önce sınandı ardından da ortak merkezli olmayan radomlar incelendi.

Anahtar sözcükler: Silindirik yansıtıcı antenler, radyasyon, radom, ikili seri denklemleri.

ACKNOWLEDGMENT

I would like to express my deep gratitude to Prof. Dr. Ayhan Altıntaş and Dr. Alexander I. Nosich for their suggestions, help and invaluable guidance during the development of this thesis.

I would also like to thank Vladimir Yurchenko for his suggestions and help.

Contents

1 INTRODUCTION 1

2 COMPLEX SOURCE POINT METHOD 4

2.1 Formulation 4

2.2 Comparison of the complex source point and the typical aperture beam patterns 7

3 MATHEMATICAL BACKGROUND FOR RHP METHOD 9

3.1 Introduction 9

3.2 Riemann-Hilbert Problem in the Complex Variable Theory . . . 10

3.3 Solution of the Riemann-Hilbert Problem 12

3.4 Solution of Canonical Dual Series Equations 13

4 REFLECTOR IN FREE SPACE 16

4.1 Formulation of the problem 16

4.2 Approximation of a parabolic reflector by a circular one 19

4.3 Dual series equations for E and H polarization cases 20

4.4 RHP solution and symmetry splitting 22

4.5 Physical Optics solution 24

4.6 Method of Moments solution 26

4.7 Far field characteristics 26

5 REFLECTOR INSIDE A RADOME 28

5.1 Radiation in the presence of a circular radome 28

5.2 Concentric radome case 29

5.3 Nonconcentric radome case 32

6 NUMERICAL RESULTS 36

6.1 Reflector in free space 37

6.2 Directivity and radiated power 49

6.3 Reflector inside a radome 50

7 CONCLUSIONS 66

A Explicit expressions for some functions appearing in Chapter 4 68

List of Figures

2.1 Geometry of a complex-source-point model. 5

2.2 Comparison of the complex source point and the aperture beam far-field pattern of equation (2.17). ka=4 for the aperture and kb=3 for the complex source. Solid line represents the complex source point pattern and the dashed line represents the aperture beam pattern of equation (2.17). 8

3.1 Simple closed curve on the complex plane 11

4.1 Circular offset reflector antenna geometry 17

4.2 Equal-value curves of the electrical error(Δ/λ) and the reflector size(D/λ) as a function of ka and θ_{ap}. Solid curves represents constant reflector size and dashed curve represents constant electrical error. 21

4.3 Front fed symmetrical reflector antenna geometry 25

5.1 Circular reflector in the presence of concentric radome 29

5.2 Circular reflector in the presence of nonconcentric radome 33

6.1 Truncation error dependence on the matrix order, for two sample geometries: ka=100(dashed curve) and ka=150 (solid curve). θ_o=0, θ_{ap}=30^o, kb=9. 38

6.2 CPU times for both polarizations. 39

6.3 Comparison of E-Polarization radiation pattern of a parabolic reflector [2] (F/D=0.96, D=10λ) with a circular one (ka=120.57, $\theta_a p$=15°). Feed directivity parameter, kb=9.06 corresponds to a $-10.09\,dB$ edge illumination. 40

6.4 Comparison of E and H polarization radiation patterns for a front-fed symmetrical circular reflector of ka=120.57, $\theta_{ap} = 15^o$ where D=10λ and $\theta_o = \beta = 0^o$. Feed parameters are kr_o=60.28, kb=9.06($-10.09\,dB$ edge illumination). 41

6.5 Comparison of E and H polarization radiation patterns for a offset circular reflector of ka=120.57, $\theta_{ap} = 15.91^o$, $\theta_o = 22^o$ where $D = 9.77\lambda$. Feed parameters are $kr_o = 60.28$, feed beaming angle $\beta = 39^o$ and kb=11.05 corresponds to a $-9.78\,dB$ and $-10.14\,dB$ edge illuminations for lower and upper edges. 42

6.6 Comparison of the physical optics radiation patterns with the present solution for a front-fed symmetrical circular reflector of ka=120.57, $\theta_{ap} = 15^o$(D=10λ). Feed parameters are kr_o=60.28, kb=9.06($-10.09\,dB$ edge illumination): E-Polarization case. . . 43

6.7 Comparison of the physical optics radiation patterns with the present solution for the same geometry as in Figure 6.6: H-Polarization case. 44

6.8 Comparison of method of moments solution with the method of regularization result for E polarization case. Front-fed symmetrical circular reflector of ka=62.8, $\theta_a p = 29.74^o (D = 10\lambda)$. Feed parameters are kro=31.4 and kb=2.6 (-9 dB edge illumination). 45

6.9 Comparison of method of moments solution with the method of regularization result for H polarization case for the previous geometry 46

6.10 Radiation patterns of large circular offset reflector for F/D_P = 0.3, h/D=0.125 and $D = 50\lambda$ where $\theta_{ap} = 25.56^o$ and $\theta_o = 30.87^o$. Feed taper is defined with the source directivity parameter kb=5.46 corresponding to $-10\,dB$ for a half angle θ_s of 37.895°. 47

6.11 Radiation pattern comparison of PO and RHP for the beam aiming angle of 48.475° with the source directivity parameter kb=5.46 for a $-10\,dB$ half angle edge illumination. 48

6.12 Effect of the different edge taperings for E-Polarization case for a front-fed symmetrical reflector with ka=62.8, $\theta_{ap} = 29.74°$ (D=9.92λ). Feed directivity parameters, kb=3.5 and kb=5 correspond to $-13.02\,dB$ and $-18.21\,dB$ edge illuminations. 51

6.13 Effect of the different edge taperings for H-Polarization case for a front-fed symmetrical reflector with ka=62.8, $\theta_{ap} = 29.74°$ (D=9.92λ). Feed directivity parameters, kb=3.5 and kb=5 correspond to $-13.02\,dB$ and $-18.21\,dB$ edge illuminations. 52

6.14 Effect of the different aperture dimensions for E-Polarization case for a front-fed symmetrical reflector of the constant angular halfwidth $\theta_{ap} = 29.74°$. Feed directivity parameter kb=5 provides $-18.21\,dB$ edge illumination. 53

6.15 Effect of the different aperture dimensions for H-Polarization case for a front-fed symmetrical reflector of the constant angular halfwidth $\theta_{ap} = 29.74°$. Feed directivity parameter kb=5 provides $-18.21\,dB$ edge illumination. 54

6.16 Total radiated power variation with increasing aperture dimension for a front-fed symmetrical reflector of $\theta_{ap} = 15°$ and f/D=0.96. Feed directivity parameter kb=1.5 corresponds to $-1.65\,dB$ edge illumination. 55

6.17 Directivity variation with increasing aperture dimension for a front-fed symmetrical circular reflector of $\theta_{ap} = 15°$ and f/D=0.96. Feed directivity parameter kb=1.5 corresponds to $-1.65\,dB$ edge illumination. 56

6.18 Total radiated power variation with increasing feed directivity parameter kb, for $\theta_{ap} = 15°$ and ka=50 (D=3.9λ). 57

6.19 Directivity variation with increasing feed directivity parameter kb, for $\theta_{ap} = 30°$ and ka=62.8 (D=10λ). 58

6.20 Variation of the directive gain with the beam aiming angle for the circular offset reflector of $F/D_P = 0.3$, h/D=0.125 and $D = 50\lambda$ where $\theta_{ap} = 25.56°$ and $\theta_o = 30.87°$. 59

6.21 Variation of the spilloverlobe levels in dB with the beam aiming angle for the circular offset reflector of $F/D_P = 0.3$, h/D=0.125 and $D = 50\lambda$ where $\theta_{ap} = 25.56^o$ and $\theta_o = 30.87^o$. 60

6.22 The radome effect on the radiation pattern for E-Polarization case. The radome geometry is defined as $ka = 62.8$, $kc = 78.5$ and $t = 0.5\lambda_d$. The permitivity of dielectric shell is 2. Feed directivity parameter $kb = 2.6$ corresponds to a $-9.92\,dB$ edge illumination. 61

6.23 The radome effect on the radiation pattern for H-Polarization case. The radome geometry is defined as $ka = 62.8$, $kc = 78.5$ and $t = 0.5\lambda_d$. The permitivity of dielectric shell is 2. Feed directivity parameter $kb = 2.6$ corresponds to a $-9.92\,dB$ edge illumination. 62

6.24 The radome effect on the radiation pattern for E-Polarization case. The radome geometry is defined as $ka = 62.8$, $kc = 78.5$ and $t = 0.5\lambda_d$. The permitivity of dielectric shell is 2. Feed directivity parameter $kb = 5$ corresponds to a $-18.21\,dB$ edge illumination. 63

6.25 The radome effect on the radiation pattern for H-Polarization case. The radome geometry is defined as $ka = 62.8$, $kc = 78.5$ and $t = 0.5\lambda_d$. The permitivity of dielectric shell is 2. Feed directivity parameter $kb = 5$ corresponds to a $-18.21\,dB$ edge illumination. 64

6.26 The radome effect on the radiation pattern for H-Polarization case. The radome is nonconcentrically located. The radome geometry is defined as $ka = 31.4$, $kc = 27.3$, $kL = 27.3$ and thickness of the radome is $t = 0.5\lambda_d$ (dashed curve) and $t = 0.4\lambda_d$ (dotted curve). The permitivity of dielectric shell is 2. Solid curve represents the reflector in free space. Feed directivity parameter $kb = 2.6$ corresponds to a $-9\,dB$ edge illumination. . 65

Chapter 1

INTRODUCTION

High frequency techniques such as the Aperture Integration (AI) and the Geometrical Theory of Diffraction (GTD) are commonly employed for predicting the far-field radiation characteristics of electrically large reflector antennas. In the papers of Suedan and Jull [1,2], it is demonstrated that the Complex Source Point (CSP) method can be successfully used in combination with AI or GTD to take account of source directivity in reflector antenna simulations, since the replacement of the real coordinate of a uniform source with the complex one generates a beam field in real space [3]. However, both AI and GTD have well-known internal shortcomings for reflector antenna problems. The former gives less accurate results off the main beam, and completely fails in shadow region. The latter, oppositely, is not applicable in the main beam direction. That is why, usually, one has to compose the results of two methods, without any clear rule of choosing the matching point. Although these high frequency techniques are applicable to many practical problems, the range of validity of the results, in terms of acceptable accuracy is unpredictable.

Provided that the reflector is not electrically large, more accurate results can be obtained by numerical techniques, such as method of moments (MoM). Normally the matrix size involved in computations with this method is 10 to 30 times the parameter D/λ, where D is the reflector dimension and λ is the wavelength. If the entire-domain basis functions are used [4], the matrix size can be smaller but the matrix filling time increases impressively. In any case, the accuracy and convergence properties are quite dependent of the implementation.

Therefore, there is still a need for a technique for the analysis and simulation of the reflector antennas with any desired accuracy. We present such a technique for circular cylindrical reflectors in which the dual series formulation

is used in combination with the complex source point approach. The aim is to demonstrate the unique opportunities offered by using this combination.

In the core of the analysis, there is the idea of regularization, i.e., a partial inversion of original integral operator. In our treatment, the inverted part of the integral operator is its static part. First, we reduce the problem to dual series equations [5-8] for surface current expansion coefficients. Then, we extract certain canonical equations and solve them exactly using Riemann-Hilbert Problem technique. The details of this approach, as it is used here, can be found in the references [5-8]. The resulting matrix equations enable one to conclude two facts of primary importance. First, the exact solution to the infinite matrix equation really exists, and second, it can be approximated with a desired accuracy (within digital precision) by solving truncated equations of large enough order. Actually, in far field computations with the uniform accuracy of 0.1%, the needed matrix size is only ka plus 5 to 10 for a realistic circular front-fed reflector of radius a.

To use the dual series approach for the simulation of reflector antennas, one has to restrict the reflector geometry to a circular cross-section. Although actual reflectors are of parabolic shape, the aperture dimensions compared to focal distance are often rather small. This offers a way to approximate the parabola by a part of a circle with great accuracy, and thus to avoid the modification of the method.

To protect the reflector antenna system from the enviromental conditions, radomes are commonly used. The performance of the reflector antenna is changed by the presence of the radome, however almost distortionless transmission is possible if the radome satisfies some electromagnetic requirements. The reflector antenna covered by a radome is analyzed by the method developed in this thesis. Normally, it is not easy to obtain the exact reference data for the given reflector and radome geometries by the other numerical methods like the method of moments. The present method gives, however, the exact solutions to the problems with any desired accuracy. By using the solutions, the far field radiation patterns as well as the directivity and the total radiated power are evaluated for the different radome and reflector electrical and geometrical parameters.

The outline of the thesis is as follows. In Section 2 following the introduction, the complex source point method is described and compared with the typical aperture beam approach. In Section 3, a mathematical background for the Riemann-Hilbert Problem technique is discussed. In Section 4, this

technique is used to solve the problem of a 2D circular reflector in the free space for both E- and H-polarization cases. The given approach is compared with the conventional physical optics and method of moments solutions, and the formulas for various far-field characteristics are presented. The similar but more complicated problem of the reflector inside a concentric or nonconcentric 2D circular dielectric radome is considered in Section 5. The numerical results for all the problems are presented in Section 6, and the concluding remarks are summarized in the final Section.

The time dependence e^{-iwt} is assumed and omitted throughout the further analysis.

Chapter 2

COMPLEX SOURCE POINT METHOD

2.1 Formulation

In a homogeneous unbounded medium, replacement of the line source position from real to complex one, creates a beam field in two dimensions (2D). This implies that complex source point(CSP) substitution converts line source Green's functions into field solutions for incident directive beams. Thus, without further effort, the whole diffraction solutions yield the field response for beam excitation, provided there can be analytic continuation of the solutions from real space to complex space.

Figure 2.1 shows a 2-dimensional line source at (r_o,θ_o) from the origin of coordinates. The fields are uniform in the z direction and represent an omnidirectional cylindrical wave. The field intensity at any observation point r,θ which is a solution of the wave equation may be written as

$$u^{in}(\vec{r}) = \frac{i}{4} H_o^{(1)}(kR) \simeq \frac{i}{4}\sqrt{\frac{2}{\pi}}\epsilon^{-i\frac{\pi}{4}} \frac{\epsilon^{ikR}}{\sqrt{kR}}, \qquad kR >> 1 \qquad (2.1)$$

where $k = w/c$ and $H_o^{(1)}$ is the Hankel function of the first kind and R is the distance of the observation point from the source,

$$R = \sqrt{r^2 + r_o^2 - 2rr_o\cos(\theta - \theta_o)}. \qquad (2.2)$$

In the far field ($r >> r_o$), $R = r - r_o\cos(\theta - \theta_o)$ applies in the phase term and R $\sim$ r in the amplitude term of (2.1) giving

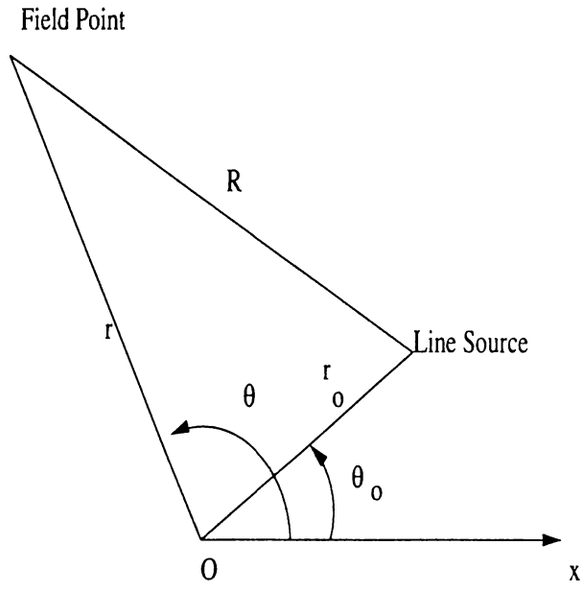

Figure 2.1: Geometry of a complex-source-point model.

$$u^{in}(r,\theta) = C\frac{e^{ik(r-r_o\cos(\theta-\theta_o))}}{\sqrt{kr}} \qquad 0 < \theta_o < \pi \tag{2.3}$$

where C is the complex constant.

By making the source coordinates (r_o, θ_o) complex (r_s, θ_s), one converts the omnidirectional wave into a directive beam uniform in the z direction. Here,

$$\vec{r_s} = \vec{r_o} + i\vec{b} \tag{2.4}$$

$\vec{r_s}$,$\vec{r_o}$ and $\vec{b}$ are the complex source position, real source position and beam parameter vectors given in polar coordinates as $\vec{r_o}=(r_o,\theta_o)$, $\vec{r_s}=(r_s,\theta_s)$ and $\vec{b}=(b,\beta)$, where b defines the sharpness of the beam and β defines its orientation. All angles are measured from the x-axis. The values of r_s and θ_s are [1,2]

$$r_s = \sqrt{r_o^2 + 2ir_o b\cos(\beta-\theta_o) - b^2} \qquad Re(r_s) > 0 \tag{2.5}$$

$$\theta_s = \arccos\left(\frac{r_o\cos(\theta_o) + ib\cos(\beta)}{r_s}\right) \tag{2.6}$$

where $b > 0$ and $0 \le \beta \le 2\pi$. Replacing r_o, θ_o by r_s, θ_s gives

$$u^{in}(r,\theta) = C\frac{e^{ik(r-r_s\cos(\theta-\theta_s))}}{\sqrt{kr}} \qquad r >> |r_s| \tag{2.7}$$

$$r_s\cos(\theta-\theta_s) = r_s\cos(\theta_s)\cos(\theta) + r_s\sin(\theta_s)\sin(\theta) \tag{2.8}$$

$$r_s\cos(\theta_s) = r_o\cos(\theta_o) + ib\cos(\beta) \tag{2.9}$$

$$r_s \sin(\theta_s) = r_o \sin(\theta_o) + ib \sin(\beta) \tag{2.10}$$

Using these in (2.8) yields

$$r_s \cos(\theta - \theta_s) = r_o \cos(\theta - \theta_o) + ib \cos(\theta - \beta) \tag{2.11}$$

Substituting (2.11) in (2.7) we get

$$u^{in}(r,\theta) = C \frac{e^{ik(r - r_o \cos(\theta - \theta_o))}}{\sqrt{kr}} e^{kb \cos(\theta - \beta)} \tag{2.12}$$

By comparing equation (2.12) with (2.3) we find that (2.12) represents an omnidirectional cylindrical wave (first term) modulated by a beam pattern $e^{kb\cos(\theta-\beta)}$ with its maximum in the direction $\theta = \beta$ and minimum in the direction $\theta = \beta + \pi$.

The incident field due to the line source of amplitude C at the complex position $\vec{r_s}$ is given by

$$u^{in}(\vec{r}) = C H_o^{(1)}(k|\vec{r} - \vec{r_s}|). \tag{2.13}$$

With the use of the addition theorem for the Hankel functions, it can be written as

$$u^{in}(r,\varphi) = C \sum_{n=-\infty}^{\infty} J_n(kr_s) H_n^{(1)}(kr) e^{in(\varphi - \theta_s)} \qquad r > |\vec{r_s}| \tag{2.14}$$

For the reflector antenna geometries, an important parameter is the total radiated power P normalized to the radiated power P_0 of the complex line source in free space. P_0 is easily found by integrating the squared absolute value of the function (2.13) over the circle of a large enough radius $k|\vec{r} - \vec{r_0}| >> 1$, and is given by

$$P_0 = C^2 \frac{2\eta}{k} I_0(2kb) \tag{2.15}$$

where η is $(Z_0)^{-1}$ and Z_0 for E and H-polarization cases, respectively. Z_0 is the intrinsic impedance of free space and I_0 is the modified Bessel function of order 0.

2.2 Comparison of the complex source point and the typical aperture beam patterns

We normalize the field of (2.12) to its peak value

$$|\frac{u^{in}(r,\theta)}{u^{in}(r,\beta)}| = e^{-kb(1-\cos(\theta-\beta))} \tag{2.16}$$

In the far zone, equation (2.13) behaves like equation (2.16). Therefore, at far zone, we use equation (2.11) as the complex source point field. Furthermore, complex source point field behaves as a Gaussian beam in the paraxial region.

Typical aperture beam pattern is an inphase cosinusoidal distribution in an aperture of width 2a. Its normalized pattern is

$$|\frac{u^{in}(r,\theta)}{u^{in}(r,\beta)}| = \frac{\cos(ka\sin(\theta-\beta))}{1-(\frac{2ka}{\pi}\sin(\theta-\beta))^2}, \tag{2.17}$$

and for ka=4, its half-power beamwidth is 55.7^o.

One can plot the beam patterns for the aperture of width 2a, as given in (2.17) with the pattern of the complex source given in (2.16) to get a comparison. For this purpose, the beamwidths of two patterns are equated using parameter "a" for the aperture and "b" for the complex source. Such a comparison is shown in Figure 2.2 . Obviously, complex source point method gives pattern for whole space although typical aperture beam patterns are only for a half space that field radiates. Therefore, plots are taken in the region of $(-90^o, 90^o)$ angles. There are two curves in Figure 2.2, solid line for complex source point pattern, dashed curve for typical aperture beam pattern. Two curves overlap in the paraxial region ($|\theta-\beta|$ small). At angles well off the beam axis, there is some difference, specially for broad beams (kb small). In addition, complex source point curve satisfies Maxwell equations in each point.

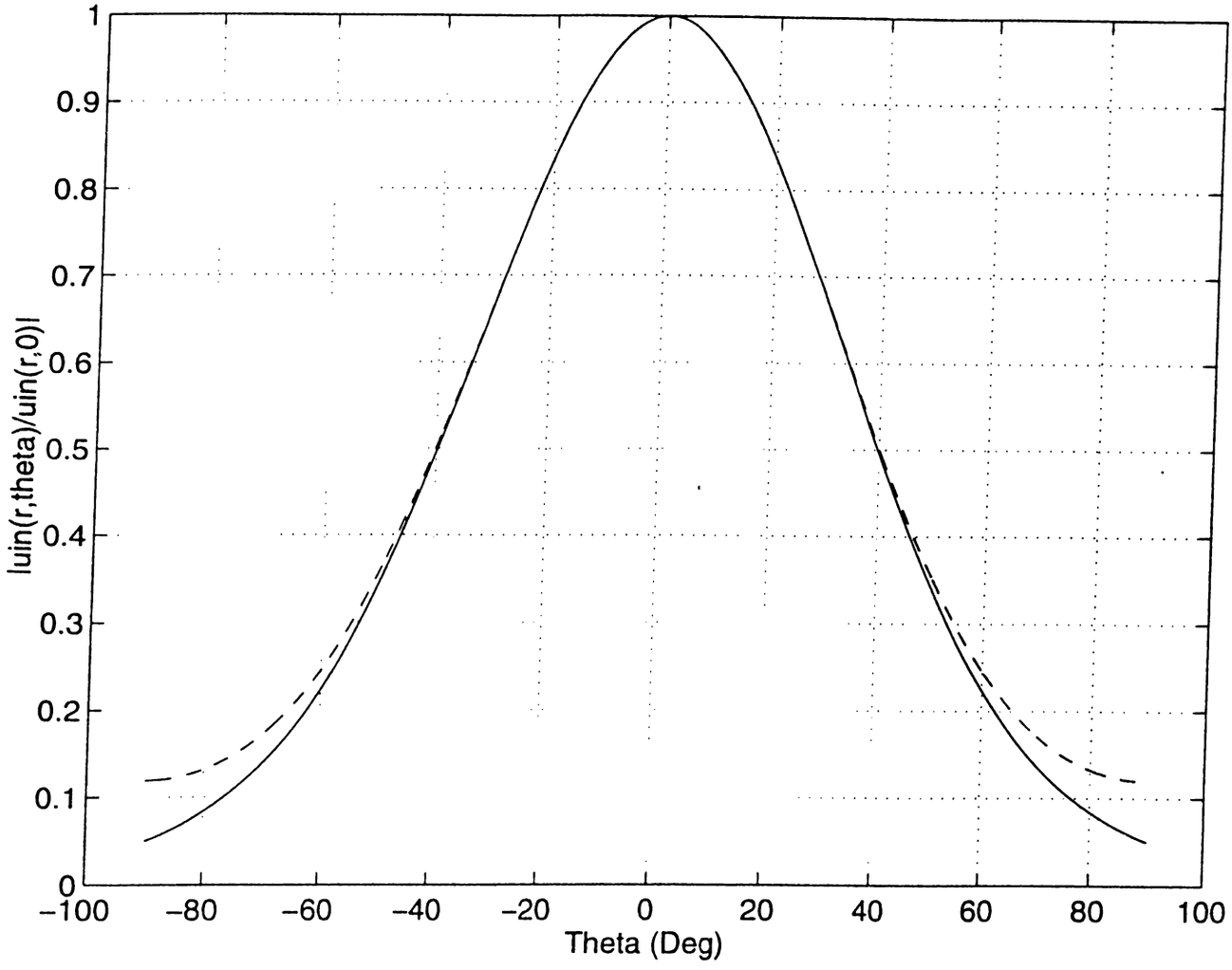

Figure 2.2: Comparison of the complex source point and the aperture beam far-field pattern of equation (2.17). ka=4 for the aperture and kb=3 for the complex source. Solid line represents the complex source point pattern and the dashed line represents the aperture beam pattern of equation (2.17).

Chapter 3

MATHEMATICAL BACKGROUND FOR RHP METHOD

3.1 Introduction

The Riemann-Hilbert problem(RHP) technique of complex variable theory makes it possible to obtain analytical solutions to canonical wave scattering and diffraction problems. Examples of canonical problems solvable with this technique include a plane wave incidence on a circular cylinder with an infinite axial slot. Due to periodicity of boundaries, all the problems can be rearranged in the form of dual series equations with the set of functions $e^{in\varphi}$, n=0,$\pm$1, ... as the kernel.

Two dimensional wave scattering problems can be reduced to singular integral equations by using a generalized potential theory approach so the Fredholm theory of integral equations is of great importance. Besides, the theory of Fourier transforms and functions of complex variable enables one to solve integral equations of certain class. This approach called the Wiener-Hopf (WH) technique. One delivers exact solutions of such canonical diffraction problems for a semiinfinite zero-thickness plate and produces effective approximate solutions for a great number of modified geometries. All these problems are known to be rearrangable in the form of equivalent dual integral equations.

The development of the Riemann-Hilbert Problem approach can be considered as another breakthrough in diffraction theory since 1960's, although it is still less known in the West than in the Soviet Union. In this chapter, the approach descriped by A.I. Nosich[8] is used. The work in [8] is mainly concerned

with combined resonant scatterers, but the RHP approach is extensively descriped. According to the approach there lies a problem about a reconstruction of an analytical function X(z) of complex variable $z = x + iy$ whose limiting values $X^{\pm}(z)$ from inside and outside of a closed finite or infinite curve L in z-plane satisfy the following condition

$$X^{+}(z_o) - A(z_o)X^{-}(z_o) = B(z_o), \qquad z_o \in L \tag{3.1}$$

with known functions $A(z_o)$ and $B(z_o)$ called the coefficient and the free term of RHP, respectively.

In this chapter, a brief explanation on the theory of analytical functions of complex variable and Cauchy type integrals is given, since Riemann-Hilbert problem is concerned with finding an analytical function that satisfies a prescribed transition condition on an open or closed curve.

3.2 Riemann-Hilbert Problem in the Complex Variable Theory

Consider a simple closed, smooth curve L which divides the complex plane into two domains $Q^{\pm}$ such that $Q^{+} = extL$ and $Q^{-} = intL$. Let X(z) be a sectionally analytic function such that X(z)=$X^{\pm}(z)$ for $z \in Q^{\pm}$. If we assume that X(z) vanishes at infinity, and also satisfies the transition condition

$$X^{+}(z_o) - X^{-}(z_o) = B(z_o), \qquad z_o \in L \tag{3.2}$$

with at least Hölder continuous function of position on that contour, and B(z_o) is a known function usually denoted as the free term, then the Cauchy integral

$$X(z) = \frac{1}{2\pi i}\int_L \frac{B(z_o)}{(z_o - z)}dz_o \tag{3.3}$$

gives the solution. For such integrals, the Plemelj-Sokhotskii formulas are valid

$$X^{\pm}(z_o) = X(z_o) \pm \frac{1}{2}B(z_o) \tag{3.4}$$

The RHP is a generalized version of this problem. Another known function $A(z_o)$ is also introduced which is also Hölder continuous function on the curve L, such that X(z) satisfies the following transition condition

$$X^{+}(z_o) - A(z_o)X^{-}(z_o) = B(z_o). \tag{3.5}$$

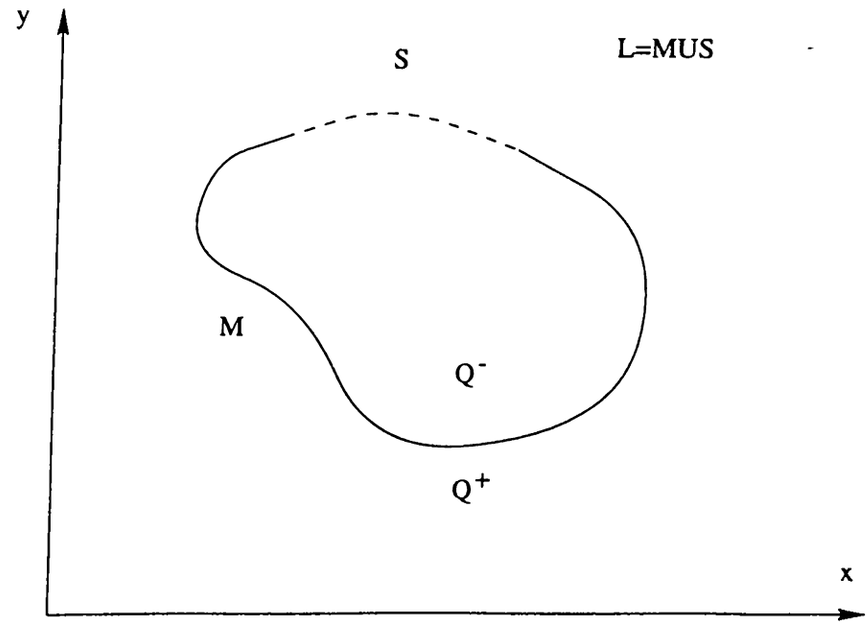

Figure 3.1: Simple closed curve on the complex plane

A further generalization of this problem is possible by introducing discontinuous coefficients, A(z_o)and B(z_o) in (3.5). In addition, the behavior of X(z) at infinity can also be modified. For instance, it may also be described by a polynomial function of z. Let, the curve L be divided into two sets, M and S, such that MUS=L, as shown in Figure 3.1. Consider a boundary value problem of finding an analytic function X(z) with the boundary expressions

$$X^+(z_o) + X^-(z_o) = B(z_o), \qquad z_o \in M, \tag{3.6}$$

$$X^+(z_o) - X^-(z_o) = 0 \qquad z_o \in S. \tag{3.7}$$

The two equations in (3.6) and (3.7) can be rearranged as a single one as

$$X^+(z_o) - \tilde{A}(z_o)X^-(z_o) = \tilde{B}(z_o) \tag{3.8}$$

by introducing discontinuous coefficient and free term functions

$$\tilde{A}(z_o) = \begin{cases} -1, & z_o \in M \\ +1, & z_o \in S \end{cases} \tag{3.9}$$

$$\tilde{B}(z_o) = \begin{cases} B(z_o), & z_o \in M \\ 0, & z_o \in S \end{cases} \tag{3.10}$$

Note that equation (3.8) is valid on the whole closed contour L.

To make further derivations, it is necessary to specify the behavior of the unknown function X(z) at infinity and at the end points of the open curve

M where $\check{A}(z)$ and $\check{B}(z)$ becomes discontinuous. It is assumed that X(z) has singularities of order 1/2 at each of the end points and is zero at infinity, which is a typical behavior for the electromagnetics problems of wave scattering and diffraction by perfectly conducting zero thickness slitted cylinders. However, the RHP technique can actually handle solutions with other singularities of the order less than 1, with nonzero behavior at infinity.

3.3 Solution of the Riemann-Hilbert Problem

By making the assumptions introduced in the previous section, we can define a function R(z), which is also called characteristic function, such that the multiplication of R(z) with X(z) becomes nonsingular everywhere, i.e. regular on the whole complex plane. It is given as

$$R(z) = (z - \alpha_1)^{1/2}(z - \alpha_2)^{1/2} \tag{3.11}$$

where z=$\alpha_{1,2}$ are the endpoints, and the branch is chosen such that brunch-cut is from α_1 to α_2 along M. Then the limit values as $z \to z_o \in M$ of R(z) differ by sign, i.e. R(z)$\to R^{\pm}(z_o) = \pm R^{+}(z_o)$.

By introducing functions Y(z) and $D(z_o)$ such that

$$Y(z) = X(z)R(z) \tag{3.12}$$

$$D(z_o) = \check{B}(z_o)R^{+}(z_o) \tag{3.13}$$

we come to a RHP with continuous coefficient function on the closed curve L

$$Y^{+}(z_o) - Y^{-}(z_o) = D(z_o). \tag{3.14}$$

Since the characteristic function has a simple pole at infinity, the solution of (3.14) is given as

$$Y(z) = \frac{1}{2\pi i}\int_L \frac{D(z_o)}{(z_o - z)}dz_o + C \tag{3.15}$$

The equation (3.15) can be written for the function X(z)

$$X(z) = \frac{1}{2\pi i}\frac{1}{R(z)}\int_M \frac{R^{+}(z_o)B(z_o)}{(z_o - z)}dz_o + \frac{C}{R(z)} \tag{3.16}$$

which is exact solution of the initial Riemann-Hilbert problem (3.6) and (3.7) with the restricted behavior of X(z) at the infinity and singularities of order 1/2 at the endpoints of the curve M.

3.4 Solution of Canonical Dual Series Equations

Consider the dual series equations with trigonometric kernel for the infinite sequence of coefficients x_n, n=0,±1, ... , given as

$$\sum_{n=-\infty}^{\infty} x_n|n|e^{in\varphi} = F(e^{i\varphi}), \qquad \varphi \in M = (|\varphi| < \theta) \tag{3.17}$$

$$\sum_{n=-\infty}^{\infty} x_n e^{in\varphi} = 0, \qquad \varphi \in S = (\theta < |\varphi| \leq \pi). \tag{3.18}$$

These dual series equations can be solved by converting the problem into a Riemann-Hilbert problem. Assuming that the series in (3.18) is term-by-term differentiable, we replace it with the derivative with respect to φ. Then we have the following equations

$$\sum_{n=-\infty}^{\infty} x_n|n|e^{in\varphi} = F(e^{i\varphi}), \qquad \varphi \in M \tag{3.19}$$

$$\sum_{n=-\infty}^{\infty} x_n n e^{in\varphi} = 0, \qquad \varphi \in S \tag{3.20}$$

$$\sum_{n=-\infty}^{\infty} x_n e^{in\pi} = 0. \tag{3.21}$$

The last equation is obtained by substituting $\varphi = \pi$ into (3.18) to account for the elimination of the constant term due to differentiation.

By introducing functions $X^{\pm}(z)$ of complex variable $z = re^{i\varphi}$ such that

$$X^{+}(z) = + \sum_{n=1}^{\infty} x_n n z^n, \quad \text{analytic in } Q^{+} = \{z : |z| < 1\} \tag{3.22}$$

$$X^{-}(z) = - \sum_{n=-\infty}^{-1} x_n n z^n, \quad \text{analytic in } Q^{-} = \{z : |z| > 1\} \tag{3.23}$$

we obtain a functional equation valid on the whole unit circle $|z| = 1$

$$X^{+}(e^{i\varphi}) - AX^{-}(e^{i\varphi}) = B \tag{3.24}$$

with known but discontinuous coefficient and free term functions

$$A(\varphi) = \begin{cases} -1, & \varphi \in M \\ +1, & \varphi \in S, \end{cases} \tag{3.25}$$

$$B(\varphi) = \begin{cases} F(e^{i\varphi}), & \varphi \in M \\ 0, & \varphi \in S. \end{cases} \tag{3.26}$$

To arrive at the exact solution of (3.24), it is necessary to restrict the behavior of the unknown function $X(z)$ at the infinity and at the end points of the screen. By assuming that $X(z)$ vanishes as $|z| \to \infty$, and has a square root singularity at the endpoints, $z = e^{\pm i\theta}$, the solution is given by the equation (3.16). By using Plemelj-Sokhotskii formulas for the limiting values of the $X(z)$, we obtain

$$X^+(t_o) - X^-(t_o) = \frac{Q(t_o)}{i\pi} \int_S \frac{R^+(t)F(t)}{(t - t_o)} dt + 2CQ(t_o) \tag{3.27}$$

where $t, t_o \in L$ and

$$Q(t_o) = \begin{cases} [R^+(t_o)]^{-1}, & t_o \in M \\ 0, & t_o \in S. \end{cases} \tag{3.28}$$

The definition in (3.22) and (3.23) yields

$$X^+(t_o) - X^-(t_o) = \sum_{(n)} n x_n e^{in\varphi}. \tag{3.29}$$

By taking the Fourier inversion of (3.29), we obtain

$$m x_m = V_m(F, \theta) + 2C R_m(\theta), \quad m = 0, \pm 1, \ldots \tag{3.30}$$

where

$$V_m(F, \theta) = \frac{1}{2\pi} \int_0^{2\pi} Q(e^{i\psi_o}) V(F, e^{i\psi_o}) e^{-im\psi_o} d\psi_o = \frac{1}{2\pi} \int_M \frac{V(F, e^{i\psi_o}) e^{-im\psi_o}}{R^+(e^{i\psi_o})} d\psi_o$$

$$V(F, e^{i\psi_o}) = \frac{1}{i\pi} P.V. \int_M \frac{R^+(t)F(t)}{t - e^{i\psi_o}} dt$$

$$R_m(\cos(\theta)) = \frac{1}{2\pi} \int_0^{2\pi} Q(e^{i\psi_o}) e^{-im\psi_o} d\psi_o = \frac{1}{2\pi} \int_M \frac{e^{-im\psi_o}}{R^+(e^{i\psi_o})} d\psi_o \ .$$

The constant term in (3.27) can be found by setting $m = 0$ in (3.30) as

$$C = -\frac{V_o}{2R_o} \ . \tag{3.31}$$

Assuming that the free term function has the Fourier expansion as

$$F(e^{i\psi}) = \sum_{(n)} f_n e^{i\psi n}, \tag{3.32}$$

one can obtain

$$V_m(F,\theta) = \sum_{(n)} f_n V_m^n \tag{3.33}$$

where

$$V_m^n = \frac{1}{2\pi}\int_M \frac{v_n(e^{i\psi_o},\theta)}{R^+(e^{i\psi_o})} e^{-im\psi_o} d\psi_o \tag{3.34}$$

$$v_n(t_o,\theta) = \frac{1}{i\pi} P.V. \int_M \frac{R^+(t)t^n}{t-t_o} dt \tag{3.35}$$

Therefore, the equation (3.27) can be reduced to

$$x_m m = \sum_{(n)} f_n \tilde{V}_m^n \tag{3.36}$$

where

$$\tilde{V}_m^n = V_m^n - V_o^n \frac{R_m}{R_o} \ . \tag{3.37}$$

One can find x_o as

$$x_o = -\sum_{(n)} f_n \sum_{(m\neq 0)} (-1)^m \frac{\tilde{V}_m^n}{m} \ . \tag{3.38}$$

In terms of Legendre polynomials $P_n(\cos\theta)$ the results are as follows

$$V_m^n(\cos\theta) = \frac{m+1}{2(m-n)}[P_m(\cos\theta)P_{n+1}(\cos\theta) - P_{m+1}(\cos\theta)P_n(\cos\theta)] \tag{3.39}$$

$$R_m(\cos\theta) = \frac{1}{2}P_m(\cos\theta), \qquad \tilde{V}_m^n = V_{m-1}^{n-1} \tag{3.40}$$

$$\sum_{m\neq 0}(-1)^m \frac{V_{m-1}^{n-1}(\cos\theta)}{m} = \begin{cases} -(1/n)V_{n-1}^{-1}(\cos\theta), & n \neq 0 \\ ln\frac{1+\cos\theta}{2} & n = 0 \ . \end{cases} \tag{3.41}$$

Thus, the final solution to the canonical dual series equations obtained by the Riemann-Hilbert Problem method is found as

$$x_m = \sum_{(n)} f_n T_{mn}(\cos\theta) \tag{3.42}$$

where $T_{mn}(\cos\theta)$ is given in the appendix.

The Riemann-Hilbert Problem method described above was first introduced in the diffraction theory by Agranovich, Marchenko and Shestopalov [5] who applied it for solving a particular plane-wave scattering problem. Later, this method was expanded for a great variety of the scattering problems by many authors. A helpful survey of the approach with its application to a number of typical problems could be found in the work [8].

Chapter 4

REFLECTOR IN FREE SPACE

4.1 Formulation of the problem

A general two-dimensional (2-D) reflector antenna geometry is shown in Figure 4.1. The perfectly-conducting reflector M is a part of a circle of radius a. The reflector has zero thickness and angular width $2\theta_{ap}$ with the central point at θ_0 which is the offset angle. For a front-fed symmetrical reflector, $\theta_0 = 0$. Geometrical focus is located at the half distance of the circular radius a, h is the offset height, ψ_L and ψ_U are subtended angles to the lower and upper edges, respectively, ψ_S is the half-angle subtended to the lower and upper edges, i.e. $(\psi_U - \psi_L)/2$.

The radiation pattern of a directive line source feed is characterized by using the CSP method as described in chapter 2. It is known that main radiation beams of most antennas are Gaussian near the beam axis, and so, the idea of analytic continuation of the real source position to the complex space has been found to be extremely fruitful. In our structure, the source is placed at the geometrical focus, i.e., $\vec{r}_0 = \frac{a}{2}\vec{a}_x$ in real space, and its directivity is characterized by $\vec{b}$, so that the complex position vector becomes

$$\vec{r}_s = \vec{r}_o + i\vec{b} = \frac{a}{2}\vec{a}_x + ib(\cos\beta\vec{a}_x + \sin\beta\vec{a}_y). \tag{4.1}$$

The real number b is a measure of the feed directivity and the aiming angle β measured from the x-axis represents the beam direction. For the front-fed reflector case, $\beta = 0$.

Depending on the polarization, we denote by $u(\vec{r})$ the H_z or E_z component of the field. The total field $u^{tot}(\vec{r})$ can be written as the sum of the incident $u^{in}(\vec{r})$ and the scattered $u^{sc}(\vec{r})$ fields. The incident field due to the line source

of amplitude C at the complex position $\vec{r_s}$ is given by

$$u^{in}(\vec{r}) = C H_0^{(1)}(k|\vec{r} - \vec{r_s}|) \tag{4.2}$$

where $k = \omega/c$, and $H_0^{(1)}(kr)$ is the Hankel function of the first kind (See section 2.1). With the use of the addition theorem for the Hankel functions, it can be written as

$$u^{in}(r,\varphi) = C \sum_{n=-\infty}^{\infty} J_n(kr_s) H_n^{(1)}(kr) e^{in(\varphi-\theta_s)}, \quad r > |\vec{r_s}| \tag{4.3}$$

where

$$r_s = \sqrt{r_0^2 + 2ir_o b\cos\beta - b^2}, \qquad \theta_s = \cos^{-1}\left(\frac{r_0 + ib\cos\beta}{r_s}\right), \quad Re(r_s) > 0. \tag{4.4}$$

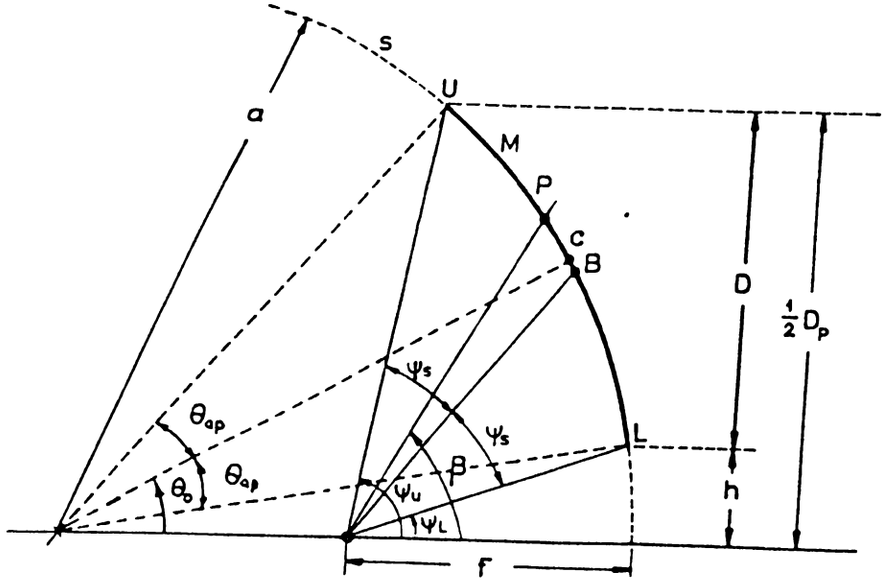

Figure 4.1: Circular offset reflector antenna geometry

For some geometries, the reflector surface may be in the near zone of the feed antenna, but the expression (4.3) is valid both at near and far zone of the feed as far as $r > |r_s|$ is satisfied. A note should be made that the function (4.2) is an exact solution of the Helmholtz equation; this is unlike Gaussian-type exponents frequently used to represent beam waves.

To obtain the rigorous solution of the problem, the scattered field has to satisfy the Helmholtz equation, the Neumann or Dirichlet type boundary condition on the screen depending on the H or E-polarization, the Sommerfeld radiation condition, and the Meixner condition at the reflector edges. These requirements guarantee the uniqueness of the solution, and moreover, the existence in a certain class of functions [10, p.116], for any smooth open contour M.

The scattered fields can be expressed in integral form as a single-layer or double-layer potential over M. Then, imposing the boundary conditions, the following equations are obtained

$$\frac{\partial H_z^{in}(\vec{r})}{\partial n} = -\frac{\partial}{\partial n}\int_M J_\varphi^H(\vec{r'})\frac{\partial}{\partial n'}G_0(\vec{r},\vec{r'})d\vec{r'}; \quad \vec{r}\in M \tag{4.5}$$

and

$$E_z^{in}(\vec{r},\vec{r'}) = -\int_M J_z^E(\vec{r'})G_0(\vec{r},\vec{r'})d\vec{r'}; \quad \vec{r}\in M \tag{4.6}$$

for H- and E-Polarization cases, respectively, where $\vec{n}$ is the outer unit normal. $J_{\varphi,z}^{H,E}(\vec{r})$ are the unknown current densities and $G_0(\vec{r},\vec{r'})$ is the 2-D Green's function (i.e., $i/4H_0^{(1)}(k|\vec{r}-\vec{r'}|)$) and define the kernel of the integral equations.

Equations (4.5) and (4.6) are widely known, as well as the MoM-based solutions of them. It is worth noting that to reduce the singularity of the kernel, (4.5) can be transformed into a form similar to (4.6) [11, p.67]. However, conventional MoM solutions using sub-domain triangle or pulse basis functions lead to matrices of the order $N = 10D/\lambda$ to $30D/\lambda$. A more reasonable choice of basis functions, like a series of sinusoids as in [4], may result in a much smaller matrix size; but it also increases the filling time drastically due to massive numerical integrations for matrix elements found as certain inner products. In general, as (4.6) is a Fredholm equation of the 1-st kind, it is ill-posed; and so the convergence of direct solutions to it is not guaranteed when $N \to \infty$.

For these reasons, it is recommended to regularize (4.5) and (4.6), i.e., to convert them to the Fredholm form of the 2-nd kind. A most straightforward way to achieve this is to make use of Tikhonov's numerical self-regularization approach. This idea was exploited in [11] for a number of 2-D and 3-D axially-symmetrical open surfaces. Here, the convergence of MoM-type algorithms is ensured. Nonetheless, all the previous remarks about the matrix size (at least $10D/\lambda$) and CPU time are valid.

The indicated problems can be overcome provided that the analytical regularization can be performed. The basic idea is of extracting a certain part of the integral operator which is invertible analytically, and inverting numerically the remaining part. Regularization ensures the existence of an exact solution and justifies application of a MoM-like numerical algorithm which is stable and has a pointwise convergence. As for the efficiency, i.e., memory requirements and CPU time, it depends on the scatterer shape which determines the matrix elements. In case of M being an open circular contour, all the matrix elements can be obtained explicitly. This procedure is equivalent to a judicious choice

of basis functions in MoM-solution (as special series of trigonometric functions [8, p.430]) possessing orthogonality, satisfying the edge condition in term-by-term manner and allowing to take inner-product integrals analytically. If the reflector is not circular, a similar approach can be developed but the matrix elements must be found by numerical integration. Thus, the advantages of the regularization in a circular geometry compel us to apply it to practical reflectors.

4.2 Approximation of a parabolic reflector by a circular one

Parabolic reflector operation is based on the well known feature of the infinite parabolic surface to focus a plane wave to a certain fixed line. By reciprocity, if a line source is placed at the focal line, the secondary field has a planar wavefront independent of the polarization. However, if the reflector contour is only a part of a parabola, then the resulting edge spillover and diffraction cause the scattered field not to be a plane wave anymore. Instead, it is a cylindrical wave, and the total pattern contains a main beam and a number of sidelobes. To decrease the effect of edges, it is preferable to increase the reflector size, and to lower the amplitude of the primary field at the edges. In fact, this is the main reason for selecting a directive source as a feeder.

It is equally well known that if the focal distance F of a parabolic arc is large enough with respect to the reflector aperture D, this arc may be well approximated by a circular one, of the radius $a = 2F$ [12]. Let us denote the radial deviation of such a circle from the parabola (i.e., the geometrical error) as $\Delta(\theta)$ corresponding to the angular position θ. This function Δ monotonically increases with θ, so that the maximum deviation is achieved at the reflector upper edge where $\theta = \theta_{ap} + \theta_0$. Further, this discrepancy between the parabola and the circle can be expressed in terms of the wavelength, Δ/λ (this error can be called the electrical error). An engineering rule-of-thumb is that the errors smaller than $\lambda/16 = 0.06\lambda$ may be neglected [13,14]. To illustrate, Figure 4.2 presents the family of equal-value curves of Δ/λ in the plane of parameters ka and θ_{ap} for a front-fed reflector. Also, the equal-value curves of the front-fed aperture size $D/\lambda = (ka/\pi)\sin\theta_{ap}$ are presented for convenience. They indicate that the domain of validity in approximating a parabolic by a circular reflector is not restricted to electrically small reflectors. Indeed, in the case of a front-fed geometry, if $\theta_{ap} = 25^\circ$ (a deep dish) one may take ka as much as

62, that is $D = 10\lambda$. However, if $\theta_{ap} = 15^o$ (a shallow dish), the corresponding values expand to $ka = 600$ and $D = 50\lambda$. For a practical offset reflector geometry where $\theta_0 \approx \theta_{ap}$, an allowed aperture dimension is approximately half as large.

4.3 Dual series equations for E and H polarization cases

Guided by the considerations of the previous sections, we restrict our further analysis to the circular reflectors. The details of the regularization procedure has been published in [5-8]. Therefore, we shall concentrate on transforming the equation in a form suitable for an efficient numerical implementation. This is achieved by splitting the resulting matrix equations into two sets of equations corresponding to even and odd parts of the surface current.

First, we discretize the integral equations (4.5) and (4.6) and reduce them to the series equations. Thus, for a circular contour M, the surface current densities are assumed to be zero on the rest of the circle (S), and expanded in terms of a series of angular functions with coefficients $x_n^{H,E}$, as follows

$$J_{\varphi,z}^{H,E}(\vec{r}) = C\,\frac{2\alpha_{H,E}}{i\pi a}\sum_{n=-\infty}^{\infty} x_n^{H,E} e^{in\varphi} \tag{4.7}$$

where $\alpha_H = 1/k$ and $\alpha_E = 1$ to account for the differentiation in (4.5). Similarly, using the addition theorem, the Green's function can be expressed in terms of a series of angular exponents. Then, substituting all the functions into (4.5) and (4.6), applying the boundary conditions over M, and taking account of the absence of the current on S, one obtains the following dual series equations.

For H-Polarization case,

$$\sum_{n=-\infty}^{\infty} x_n^H J'_n(ka) H_n^{(1)'}(ka) e^{in\varphi} = -\sum_{n=-\infty}^{\infty} b_n^H e^{in\varphi}, \quad \varphi \in M, \tag{4.8}$$

$$\sum_{n=-\infty}^{\infty} x_n^H e^{in\varphi} = 0, \qquad \varphi \in S, \tag{4.9}$$

For E-Polarization case,

$$\sum_{n=-\infty}^{\infty} x_n^E J_n(ka) H_n^{(1)}(ka) e^{in\varphi} = -\sum_{n=-\infty}^{\infty} b_n^E e^{in\varphi}, \quad \varphi \in M, \tag{4.10}$$

$$\sum_{n=-\infty}^{\infty} x_n^E e^{in\varphi} = 0, \qquad \varphi \in s, \tag{4.11}$$

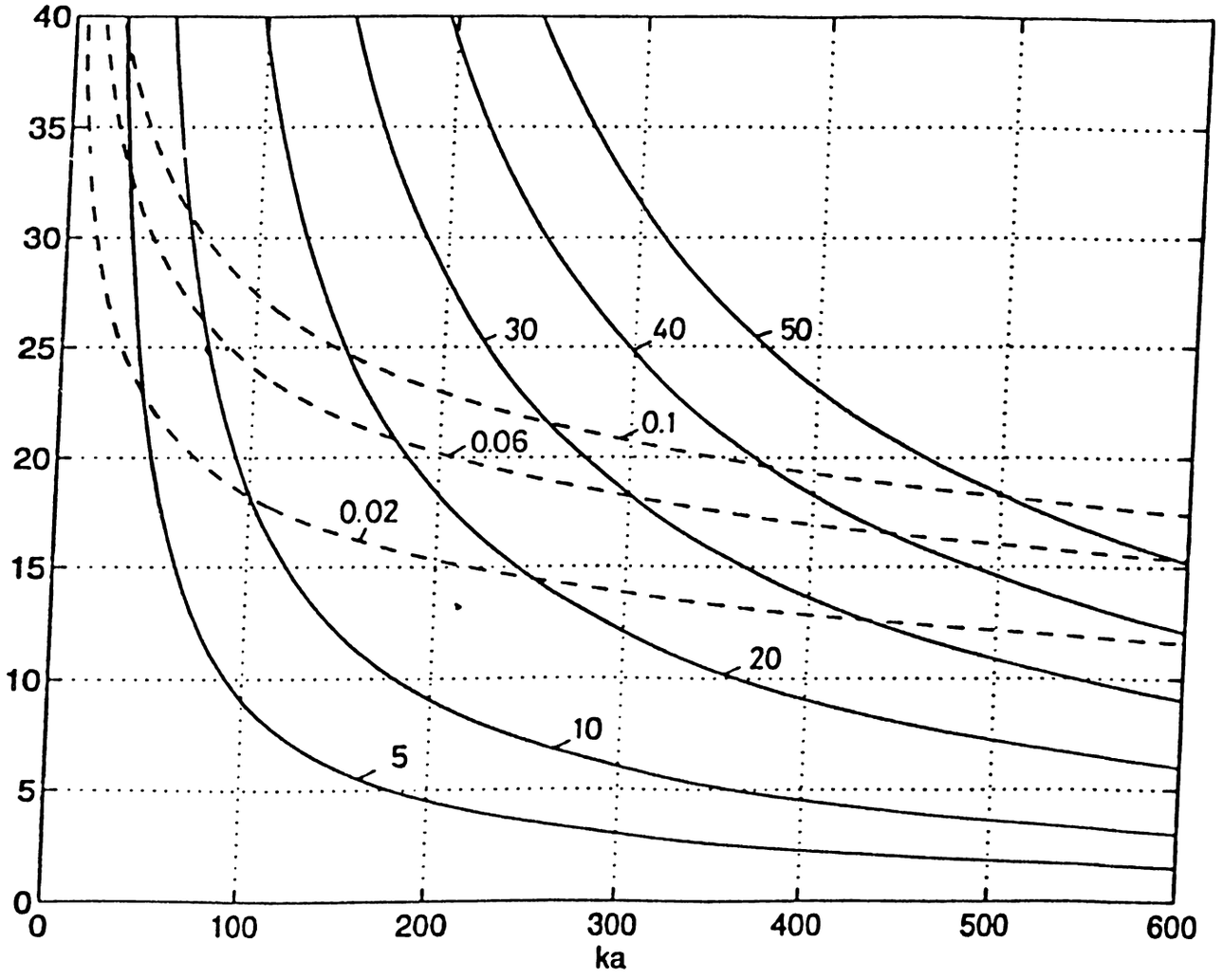

Figure 4.2: Equal-value curves of the electrical error(Δ/λ) and the reflector size(D/λ) as a function of ka and θ_{ap}. Solid curves represents constant reflector size and dashed curve represents constant electrical error.

where

$$b_n^H = J_n(kr_s)H_n^{(1)'}(ka)e^{-in\theta_s}, \qquad b_n^E = J_n(kr_s)H_n^{(1)}(ka)e^{-in\theta_s}, \tag{4.12}$$

and the prime denotes the derivative with respect to the argument.

4.4 RHP solution and symmetry splitting

One can solve the dual series equations using the point-matching method [15]. However, as we have noted previously, that approach leads to an ill-posed equation set having no proof of universal convergence. Instead, we extract a canonical form from the dual series equations which can be converted into a Riemann-Hilbert Problem. Then, the analytical solution of the latter leads to a regularized infinite algebraic equation system of the Fredholm 2-nd kind differing from the plane-wave excitation case only by the right-hand part. In terms of the integral equations (4.5) and (4.6), this procedure is equivalent to extracting and inverting the logarithmic part of the kernel function.

For H-polarization case, the regularized matrix equation is obtained as

$$x_n^H = \sum_{n=-\infty}^{\infty} \Delta_n^H T_{mn}^H e^{i(n-m)\theta_0} x_n^H + i\pi(ka)^2 \sum_{n=-\infty}^{\infty} b_n^H T_{mn}^H e^{i(n-m)\theta_0}\ , \tag{4.13}$$

and for E-polarization as

$$x_n^E = \sum_{n=-\infty}^{\infty} x_n^E(-1)^{m+n} W_{mn}^E e^{i(n-m)\theta_0} T_{mn}^E + \frac{b_m^E - \sum_{n=-\infty}^{\infty} (-1)^{m+n}|n| b_n^E e^{i(n-m)\theta_0} T_{mn}^E}{J_m(ka)H_m^{(1)}(ka)} \tag{4.14}$$

where

$$W_{mn}^E = \Delta_n^E \frac{J_n(ka)H_n^{(1)}(ka)}{J_m(ka)H_m^{(1)}(ka)}\ .$$

The equation sets (4.13) and (4.14) obtained have summations going from $-\infty$ to $+\infty$. After truncation at the term N_{tr}, they will have the order $2N_{tr}+1$. To reduce the computation time, each of them can be splitted to two independent half-size equations. This is done by decomposing the problem into even and odd parts with respect to the symmetry axis of reflector. Indeed, introducing the even and odd expansion coefficients as

$$\alpha_m^{(H,E),\pm} = (-1)^m (x_m^{H,E} e^{im\theta_0} \pm x_{-m}^{H,E} e^{-im\theta_0}) \tag{4.15}$$

and substituting (4.15) into matrix equations, one obtains

$$\alpha_m^{(H,E),\pm} = \sum_{n=(0)1}^{\infty} A_{mn}^{(H,E),even/odd}\alpha_n^{(H,E),\pm} + B_m^{(H,E),even/odd}, \quad m = (0)1,2,... \tag{4.16}$$

where

$$A_{mn}^{(H),even/odd} = (-1)^{m+n}\gamma_n^{\pm}[A_{mn}^{(H)} \pm A_{-mn}^{(H)}]. \tag{4.17}$$

$$A_{mn}^{(E),even/odd} = (-1)^{m+n}\gamma_n^{\pm}[A_{mn}^{(E)} \pm A_{-mn}^{(E)}]. \tag{4.18}$$

$$B_m^{(H),even/odd} = i\pi(ka)^2 \sum_{n=(0)1}^{\infty} b_n^{(H),even/odd}(-1)^{m+n}(T_{mn}^H \pm T_{-mn}^H), \tag{4.19}$$

$$B_m^{(E),even/odd} = \frac{-b_m^{(E),even/odd} + \sum_{n=(0)1}^{\infty} |n| b_n^{(E),even/odd}(T_{mn}^E \pm T_{-mn}^E)}{J_m(ka)H_m^{(1)}(ka)}, \tag{4.20}$$

with the coefficients $b_n^{(H),even/odd}$ and $b_n^{(E),even/odd}$ defined as follows

$$b_n^{(H),even/odd} = \gamma_n^{\pm}(-1)^n(b_n^H e^{in\theta_0} \pm b_{-n}^H e^{-in\theta_0}) \tag{4.21}$$

$$b_n^{(E),even/odd} = (-1)^n(b_n^E e^{in\theta_0} \pm b_{-n}^E e^{-in\theta_0}). \tag{4.22}$$

Here, γ_n^+ is equal to $\frac{1}{2}\delta_n$ and γ_n^- is equal to unity where δ_n is defined as 1 if n=0, otherwise 2. Other coefficients, $T_{mn}^H = T_{mn}(\cos\theta_{ap})$. $T_{mn}^E = T_{mn}(-\cos\theta_{ap})$ and the functions Δ_n^E,Δ_n^H, T_{mn}, A_{mn}^H, and A_{mn}^E are defined in the Appendix.

When solving a matrix equation, the CPU time is not a linear function of the matrix order. Therefore the reduction to two half-size equation sets saves the CPU time especially for large matrices, and also it avoids the inaccuracies resulting from the possible round off errors.

Note that in (4.16), the right hand parts have infinite summations that may lead to a certain truncation error in practical computations. The selection of new unknowns as

$$\beta_m^{(H),\pm} = \gamma_m^{\pm}\Delta_m^H\alpha_m^{(H),\pm} + i\pi(ka)^2 b_m^{H,even/odd} \tag{4.23}$$

$$\beta_m^{(E),\pm} = \gamma_m^{\pm}J_m(ka)H_m^{(1)}(ka)\Delta_m^E\alpha_m^{(E),\pm} + |m|b_m^{E,even/odd} \tag{4.24}$$

modifies (4.16) to a form which enables one to minimize the truncation error in the right hand part. Eventually, any of obtained equations can be written

in the following operator notation

$$(I - \tilde{A}^{(H,E),even/odd})\beta^{(H,E),\pm} = \check{B}^{(H,E),even/odd} \tag{4.25}$$

where

$$\tilde{A}^{(H),even/odd}_{mn} = \gamma^{\pm}_m(-1)^{m+n}\Delta^H_m(T^H_{mn} \pm T^H_{-mn}) \tag{4.26}$$

$$\tilde{A}^{(E),even/odd}_{mn} = \gamma^{\pm}_m\Delta^E_m(T^E_{mn} \pm T^E_{-mn}) \tag{4.27}$$

$$B^{(H),even/odd}_m = i\pi(ka)^2 b^{(H),even/odd}_m \tag{4.28}$$

$$B^{(E),even/odd}_m = -i\gamma^{\pm}_m[\pi J_m(ka)H^{(1)}_m(ka)]^{-1}b^{(E),even/odd}_m\ , \tag{4.29}$$

I is the identity operator, and all the operators $\tilde{A}$ are compact in the Hilbert space of infinite sequences, l_2 (i.e., with finite sum of squared absolute values of coefficients), see [8, p.430]. Hence, any of the operators $I - \tilde{A}$ is of the Fredholm 2-nd kind in l_2, and so Fredholm's theorems are valid: provided that the right-hand part also belongs to l_2, then the unique solution β exists in l_2. Large-index estimates for cylindrical functions show that $\check{B} \in l_2$ if $|r_s| < a$, resulting in a restriction $a > 2b/\sqrt{3}$ for front-fed primary line source. Furthermore, the approximate solution may be obtained with any desired accuracy via truncation to a finite order N_{tr} as the uniform pointwise convergence to exact solution is guaranteed for $N_{tr} \to \infty$.

4.5 Physical Optics solution

In the analysis of reflector antenna systems Physical Optics (PO) is a well known popular method[12,13]. PO uses Geometric Optic (GO) based currents, and generally gives better results for the mainbeam and the first few sidelobes of a parabolic reflector antenna. In the PO method, the radiation integral for the scattered field is calculated by employing the GO approximation for the currents induced on the reflector which is assumed to be electrically large. PO does yield useful estimates in directions where the GO currents produce the dominant contribution to the scattered fields. Results are obtained for both E and H polarization cases. Surface current is defined as $\vec{J_{PO}} = 2\hat{n} \times \vec{H^{in}}$ where $\hat{n}$ unit normal vector to the surface of the reflector(See Figure 4.3) and $\vec{H^{in}}$ is the incident magnetic field. Incident field depends on E or H polarization cases that is given as $\frac{e^{ik\rho_s}}{\sqrt{\rho_s}}$ where ρ_s is the complex position vector dependent on ρ which is the position vector from the source to the reflector surface,

$$\rho_s = \sqrt{\rho^2 - b^2 - 2i\rho b\cos(\theta + \beta)}. \tag{4.30}$$

Integral formulas are obtained for both E and H polarization cases as follows

H-Polarization

$$H_z = 2\sqrt{\frac{k}{8\pi}}e^{-i\pi/4}\frac{e^{ikr}}{\sqrt{r}}\int_C \cos(o+\theta/2)\frac{e^{ik\rho_s}}{\sqrt{\rho_s}}\epsilon^{-ik(x\cos(\phi)+y\sin(\phi))}dl \qquad (4.31)$$

E-Polarization

$$E_z = -e^{i\frac{\pi}{4}}\frac{e^{ikr}}{\sqrt{\lambda r}}\int_C \frac{e^{ik\rho_s}}{\sqrt{\rho_s}}\epsilon^{-ik(x\cos(o)+y\sin(\phi))}dl \qquad (4.32)$$

where

$$\rho_s = \sqrt{\rho^2 - b^2 - 2i\rho b\cos(\theta)} \qquad \beta = \pi \qquad (4.33)$$

and

$$dl = \sqrt{1+(\frac{dx}{dy})^2}dy \qquad x = \frac{y^2}{4f}. \qquad (4.34)$$

Surface current density is given by

$$\vec{J_{PO}} = 2\frac{e^{ik\rho_s}}{\sqrt{\rho_s}}(-\vec{t}) \qquad (4.35)$$

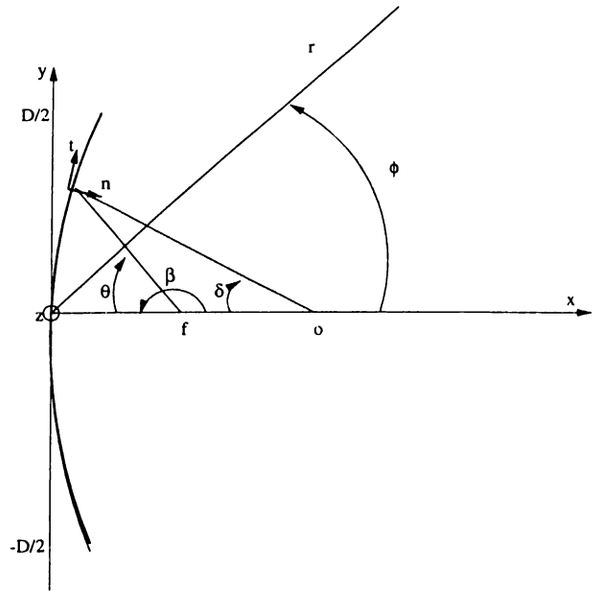

Figure 4.3: Front fed symmetrical reflector antenna geometry

Finally, integral equations become that

$$H_z = e^{-i\pi/4}\frac{e^{ikr}}{\sqrt{\lambda r}}\int_{-D/2}^{D/2}\cos(\phi+\theta/2)\frac{e^{ik\rho_s}}{\sqrt{\rho_s}}\epsilon^{-ik(\frac{y^2}{4f}\cos(\phi)+y\sin(\phi))}\frac{\sqrt{4f^2+y^2}}{2f}dy \qquad (4.36)$$

$$E_z = -e^{-i\pi/4}\frac{e^{ikr}}{\sqrt{\lambda r}}\int_{-D/2}^{D/2}\frac{e^{ik\rho_s}}{\sqrt{\rho_s}}e^{-ik(\frac{y^2}{4f}\cos(\phi)+y\sin(\phi))}\frac{\sqrt{4f^2+y^2}}{2f}dy \qquad (4.37)$$

4.6 Method of Moments solution

A method of moments solution is performed to compare the results for the circular screen with the RHP technique. Method of moments can be used in the solution of the small and medium size reflector antenna analysis. Although accuracy and convergence are not guaranteed, it may be practical to apply. A simple solution is obtained by applying point-matching method to the circular screen. Matching points are taken on the metallic and slot part of the circle.The following Dual Series Equations are used in the method of moments formulation.

For H-Polarization

$$\sum_{n=-N_{tr}}^{N_{tr}} x_n^H J_n'(ka) H_n^{(1)'}(ka) e^{in\varphi} = -\sum_{n=-N_{tr}}^{N_{tr}} b_n^H e^{in\varphi} \qquad \varphi \in M \qquad (4.38)$$

$$\sum_{n=-N_{tr}}^{N_{tr}} x_n^H e^{in\varphi} = 0 \qquad \varphi \in S \qquad (4.39)$$

For E-Polarization

$$\sum_{n=-N_{tr}}^{N_{tr}} x_n^E J_n(ka) H_n^{(1)}(ka) e^{in\varphi} = -\sum_{n=-N_{tr}}^{N_{tr}} b_n^E e^{in\varphi} \qquad \varphi \in M \qquad (4.40)$$

$$\sum_{n=-N_{tr}}^{N_{tr}} x_n^E e^{in\varphi} = 0 \qquad \varphi \in S \qquad (4.41)$$

where $b_n^H = J_n(kr_s) H_n^{(1)'}(ka) e^{-in\theta_s}$ and $b_n^E = J_n(kr_s) H_n^{(1)}(ka) e^{-in\theta_s}$.

There are $2N_{tr}+1$ unknowns in the dual series equations. Therefore $2N_{tr}+1$ points at equal angles are taken on the circle of radius a to satisfy the equations (4.38),(4.39) or (4.40),(4.41).

4.7 Far field characteristics

The radiation pattern of the primary source is obtained from (4.2) or (4.3) by using large-kr asymptotic expansions of the Hankel functions. Similarly, one obtains the total field radiation pattern in the presence of the reflector as

$$u^{tot}(r,\phi) \underset{r\to\infty}{\sim} C \left(\frac{2}{i\pi kr}\right)^{1/2} e^{ikr} \sum_{n=-\infty}^{\infty} (-i)^n [J_n(kr_s) e^{-in\theta_s} + y_n] e^{in\varphi} \qquad (4.42)$$

where y_n is taken as $x_n^H J_n'(ka)$ or $x_n^E J_n(ka)$ depending on the H or E-polarization, respectively.

For the reflector antenna geometries, an important parameter is the total radiated power P normalized to the radiated power P_0 of the complex line source in free space. P_0 is easily found by integrating the squared absolute value of the function (4.2) over the circle of a large enough radius $k|\vec{r} - \vec{r_0}| >> 1$, and is given by

$$P_0 = C^2 \frac{2\eta}{k} I_0(2kb) \tag{4.43}$$

where η is $(Z_0)^{-1}$ and Z_0 for E and H-polarization cases, respectively. Z_0 is the intrinsic impedance of free space and I_0 is the modified Bessel function of order 0.

Note that P_0 increases with kb rapidly as $e^{2kb}/\sqrt{kb}$. By following the formulation of Section 2, the expression for P/P_0 is obtained as follows

$$\frac{P}{P_0} = 1 + \frac{1}{I_0(2kb)} \sum_{n=-\infty}^{\infty} \{|y_n|^2 + 2Re[y_n^* J_n(kr_s) e^{-in\theta_s}]\}. \tag{4.44}$$

The directivity D in the main beam direction ($o = \pi$) is readily obtained as

$$D = \frac{2\eta}{kP} \left| \sum_{n=-\infty}^{\infty} i^n [J_n(kr_s) e^{-in\theta_s} + y_n] \right|^2. \tag{4.45}$$

The frequency dependence of P/P_0 and D is important in designing the narrow beam reflector antennas for pulse power transmission and wide-band communications. The directivity should be compared to the prime feed directivity, D_0, in the source beam direction ($\phi = 3$), which is easily found as

$$D_0 = I_0^{-1}(2kb) e^{2kb}. \tag{4.46}$$

The ratio D/D_0 shows the efficiency of the reflector as a directivity transformer.

Chapter 5

REFLECTOR INSIDE A RADOME

5.1 Radiation in the presence of a circular radome

To protect the reflector antenna systems from the environmental conditions, radomes are commonly used. The performance of the reflector antenna is changed by the presence of the radome, however almost distortionless transmission is possible if the radome satisfies some electromagnetic requirements. Traditional techniques for the analysis of radomes, ray-tracing [17] and plane wave spectrum-surface integration (PWS-SI) [18] methods are based on the high frequency approximations. Both approaches depend on the local planar approximation for the curved interface reflection and transmission. The antenna field at the radome walls are assumed to be a local plane wave nature as well as the radome wall is locally planar at the same point. Therefore, both methods are used for a relatively large radome whose radii of curvature are large compared to wavelength.

In the PWS-SI technique [18], plane wave spectrum approach is combined with a surface integration procedure like physical optics or aperture integration. Multiple scattering by the antenna and radome is generally ignored and only fields on the radome surface lie in the forward halfspace of the antenna is considered. Ray-optical technique is one of the earliest methods. The aperture distribution is treated as a series of rays which are traced through the radome wall. In [19] and [20], ray-optical technique is extended to include the curvature effects compared by the cylindrical radome of constant width. Radome problems can also be solved by the numerical methods like method of moments [21]. However, it is mainly limited to the small and medium size radomes.

In this section, radiation from a two dimensional circular reflector covered

by a concentric and nonconcentric dielectric radome is analyzed by complex source-dual series approach. The solution is based on Riemann-Hilbert Problem technique, therefore unlike usual method of moments the results converge to the exact one in a pointwise manner. The feed antenna is again modelled by the complex source point method.

5.2 Concentric radome case

The geometry of the problem is two dimensional circular reflector surrounded with a concentric radome as shown in Figure 5.1. The reflector is modeled by a part of a circular, zero-thickness, perfectly conducting material of the radius "a" and angular width "$2\theta_{ap}$". The feed antenna is located at the half distance of the circular radius "a" and its beam is directed to the center of the symmetric front-fed reflector. Concentric radome of the relative permittivity ϵ_r and the permeability μ_r covers the reflector system and its inner and outer radius are given by "c" and "d", respectively.

The requirements for the rigorous solution of the present boundary value problem can be stated as the satisfaction of the Helmholtz equation, Sommerfeld radiation condition, edge conditions at the reflector edges and the boundary conditions on the conducting boundary and the boundaries of the circular radome.

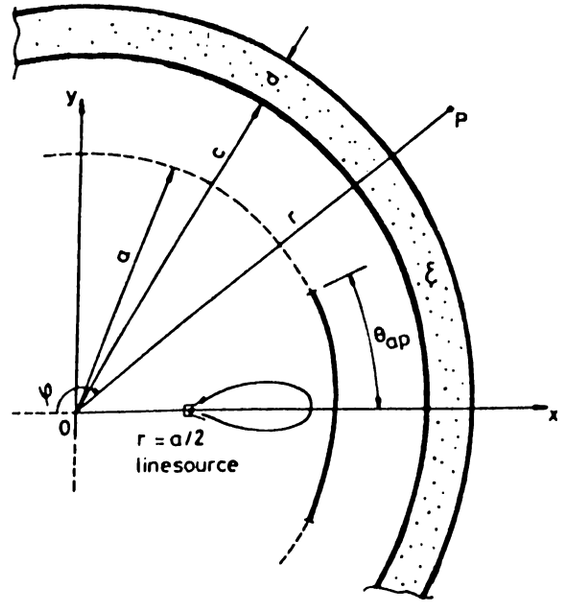

Figure 5.1: Circular reflector in the presence of concentric radome

The basic electric field integral equations (EFIE) are obtained for both polarizations by applying the boundary conditions on the reflector part. These equations are

$$\frac{\partial}{\partial n}\int_M G^H_{z\varphi}(\vec{r},\vec{r'})J^H_\varphi(\vec{r'})d\vec{r'} = -\frac{\partial}{\partial n}H^{in}_z(\vec{r})\,,\quad \vec{r}\in M\,,\quad H-Polarization \tag{5.1}$$

and

$$\int_M G^E_{zz}(\vec{r},\vec{r'})J^E_z(\vec{r'})d\vec{r'} = -E^{in}_z(\vec{r})\,,\quad \vec{r}\in M\,,\quad E-Polarization \tag{5.2}$$

where G^E_{zz} and $G^H_{z\varphi}$ are the Green's functions for the layered medium and $\vec{n}$ is the unit normal.

The Green's functions for the single radome layer can be expressed as

$$G^H_{z\varphi}(\vec{r},\vec{r'}) = G^H_o(\vec{r},\vec{r'}) + G^{sc,H}_{z\varphi}(\vec{r},\vec{r'}) \tag{5.3}$$

$$G^E_{zz}(\vec{r},\vec{r'}) = G^E_o(\vec{r},\vec{r'}) + G^{sc,E}_{zz}(\vec{r},\vec{r'}) \tag{5.4}$$

where G^H_o and G^E_o are the free space Green's functions for the z-directed magnetic (or electric) fields created by the line source located at the position (r',φ') carrying a φ-directed (or z-directed) current. These functions can be written as

$$G^H_o(\vec{r},\vec{r'}) = \frac{\partial}{\partial r'}G_o(\vec{r},\vec{r'}) = \sum_{n=-\infty}^{\infty} g^H_{on}e^{in\varphi}\,,\quad r>r' \tag{5.5}$$

$$G^E_o(\vec{r},\vec{r'}) = G_o(\vec{r},\vec{r'}) = \sum_{n=-\infty}^{\infty} g^E_{on}e^{in\varphi}\,,\quad r>r' \tag{5.6}$$

where $G_o(\vec{r},\vec{r'}) = \frac{i}{4}H^{(1)}_o(k|\vec{r}-\vec{r'}|)$ is the 2D free space scalar Green's function. The expansion coefficients are given as

$$g^H_{on} = \frac{i}{4}J'_n(k_or')H^{(1)}_n(k_or)e^{-in\varphi'}\,,\quad g^E_{on} = \frac{i}{4}J_n(k_or')H^{(1)}_n(k_or)e^{-in\varphi'}\,. \tag{5.7}$$

Let

$$G^{H,E}_{z(\varphi,z)} = \sum_{n=-\infty}^{\infty}\left\{\begin{array}{rl} D^{H,E}_nH^{(1)}_n(k_or) & d<r \\ B^{H,E}_nJ_n(kr)+C^{H,E}_nH^{(1)}_n(kr) & c<r<d \\ A^{H,E}_nJ_n(k_or)+g^{H,E}_{on} & a<r<c \end{array}\right\}e^{in\varphi}\,. \tag{5.8}$$

The expansion coefficients $A^{H,E}_n$,$B^{H,E}_n$,$C^{H,E}_n$ and $D^{H,E}_n$ are evaluated by the application of the boundary conditions.

In order to reduce the integral equations (5.1) and (5.2) to the dual series equation, we substitute the discretized equivalent of the each integral parameter. The surface current densities are expanded in terms of a series of angular functions with Fourier series coefficients $x_n^{H,E}$ as follows

$$J_{\varphi,z}^{H,E}(\vec{r}) = 2\frac{\alpha_{H,E}}{i\pi a}\sum_{n=-\infty}^{\infty} x_n^{H,E} e^{in\varphi} \tag{5.9}$$

where $\alpha_H = 1/k$ and $\alpha_E = 1$.

Then the substitution of the discretized form of the surface current density, Green's function and the incident field leads to the following dual series equations.

H - Polarization case,

$$\sum_{n=-\infty}^{\infty} x_n^H \beta_n^H e^{in\varphi} = -\sum_{n=-\infty}^{\infty} b_n^H e^{in\varphi}\ , \quad \varphi \in M \tag{5.10}$$

$$\sum_{n=-\infty}^{\infty} x_n^H \epsilon^{in\varphi} = 0\ , \quad \varphi \in S \tag{5.11}$$

E - polarization case,

$$\sum_{n=-\infty}^{\infty} X_n^E \beta_n^E e^{in\varphi} = \sum_{n=-\infty}^{\infty} b_n^E \beta_n^E e^{in\varphi}\ , \quad \varphi \in S \tag{5.12}$$

$$\sum_{n=-\infty}^{\infty} X_n^E \epsilon^{in\varphi} = 0\ , \quad \varphi \in M\ . \tag{5.13}$$

with

$$X_n^E = \frac{x_n^E}{\beta_n^E} + b_n^E\ . \tag{5.14}$$

The functions appeared in the dual series equations are defined as

$$\beta_n^H = J'_n(k_o a)H_n^{(1)'}(k_o a) - J'_n(k_o a)^2 K_n^H \tag{5.15}$$

$$\beta_n^E = (J_n(k_o a)H_n^{(1)}(k_o a) - J_n(k_o a)^2 K_n^E)^{-1} \tag{5.16}$$

where $K_n^{H,E} = \dfrac{g_n^{H,E} c_n^{H,E} - f_n^{H,E} d_n^{H,E}}{g_n^{H,E} a_n^{H,E} - f_n^{H,E} b_n^{H,E}}$

$$f_n^{H,E} = J_n(kd)H_n^{(1)'}(k_o d) - k^{H,E} J'_n(kd)H_n^{(1)}(k_o d) \tag{5.17}$$

$$g_n^{H,E} = H_n^{(1)}(kd)H_n^{(1)'}(k_o d) - k^{H,E} H_n^{(1)'}(kd)H_n^{(1)}(k_o d) \tag{5.18}$$

$$a_n^{H,E} = J_n(kc)J'_n(k_oc) - k^{H,E}J_n(k_oc)J'_n(kc) \quad (5.19)$$

$$b_n^{H,E} = H_n^{(1)}(kc)J'_n(k_oc) - k^{H,E}J_n(k_oc)H_n^{(1)'}(kc) \quad (5.20)$$

$$c_n^{H,E} = J_n(kc)H_n^{(1)'}(k_oc) - k^{H,E}H_n^{(1)}(k_oc)J'_n(kc) \quad (5.21)$$

$$d_n^{H.E} = H_n^{(1)}(kc)H_n^{(1)'}(k_oc) - k^{H,E}H_n^{(1)}(k_oc)H_n^{(1)'}(kc) \quad (5.22)$$

$$b_n^H = \frac{i}{4}J_n(k_or_s)(H_n^{(1)'}(k_oa) - J'_n(k_oa)K_n^H)e^{-in\theta_s} \quad (5.23)$$

$$b_n^E = \frac{i}{4}J_n(k_or_s)(H_n^{(1)}(k_oa) - J_n(k_oa)K_n^E)e^{-in\theta_s} \quad (5.24)$$

where k^H and k^E are defined as $k^H = \sqrt{\frac{\mu_r}{\epsilon_r}}$, $k^E = \sqrt{\frac{\epsilon_r}{\mu_r}}$.

Then, the DSE's are converted to a certain canonical form and regularized by RHP technique. The problem is reduced to an infinite matrix equation for the unknown Fourier coefficients and splitted to even and odd algebraic equation systems as described in Chapter 4. Since its operator is compact in the Hilbert space l^2[8], the truncation of the infinite matrix equation yields the solution with any desired accuracy. The resultant algebraic equation system is Fredholm second kind. Therefore, Fredholm theorems state that the solution exists and unique.

In the far field, the radiation pattern is given as

$$\phi(\varphi) = \sum_{n=-\infty}^{\infty}(R_n^{H,E}M_n^{H,E}N_n^{H,E} + \frac{i}{4}J_n(k_or_s)M_n^{H.E}N_n^{H.E}\epsilon^{-in\theta_s})(-i)^n e^{in\varphi} \quad (5.25)$$

where $R_n^H = J'_n(k_oa)x_n^H$, $R_n^E = J_n(k_oa)x_n^E$ and

$$M_n^{H,E} = k^{H,E}(J'_n(k_oc)H_n^{(1)}(k_oc) - H_n^{(1)'}(k_oc)J_n(k_oc)) \\ (J'_n(kd)H_n^{(1)}(kd) - H_n^{(1)'}(kd)J_n(kd)) \quad (5.26)$$

$$N_n^{H,E} = \frac{1}{g_n^{H,E}a_n^{H,E} - f_n^{H.E}b_n^{H,E}} \quad (5.27)$$

5.3 Nonconcentric radome case

In this case, the centers of the radome and the circular reflector do not coincide. It implies the radome is shifted with respect to the reflector by the length L. The geometry of the problem is shown in Figure 5.2. Nonconcentric radome case is performed for H-polarization.

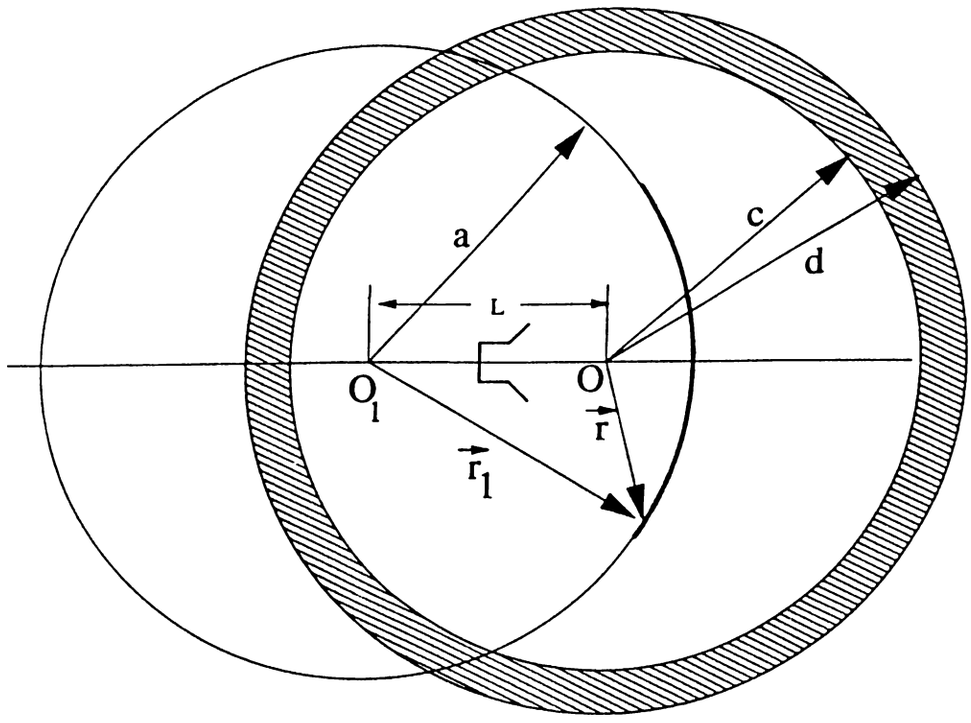

Figure 5.2: Circular reflector in the presence of nonconcentric radome

The basic electric field integral equation (EFIE) is obtained for H-polarization case by the application of the boundary conditions on the reflector part,

$$\frac{\partial}{\partial r_1}\int_M G^H_{z\varphi}(\vec{r_1},\vec{r_1'})J_\varphi(\vec{r_1'})d\vec{r_1'} = -\frac{\partial}{\partial r_1}H^{in}(\vec{r_1}) \ , \qquad \vec{r_1} \in M \ . \tag{5.28}$$

The surface current density is expanded in terms of Fourier Series coefficients as follows

$$J_\varphi(\vec{r_1'}) = \frac{2}{i\pi k_o a}\sum_{m=-\infty}^{\infty} x_m^H e^{im\varphi_1'} \ . \tag{5.29}$$

The incident field is the line source radiation in the presence of the radome,

$$\frac{\partial}{\partial r_1}H^{in}(\vec{r_1}) = \sum_{m=-\infty}^{\infty} b_n^H e^{im\varphi_1} \tag{5.30}$$

where b_n^H is given as

$$b_n^H = \frac{i}{4}J_n(k_o r_s)H_n^{(1)'}(k_o a)e^{-in\theta_s} - \frac{i}{4}J_n'(k_o a)\sum_{l=-\infty}^{\infty} J_l(k_o r_{s1})e^{-il\theta_s}L_{ln}, \tag{5.31}$$

L_{ln} is explained on the page 35, and r_{s1} is the complex source position in O_1 system.

The Green's function for the single radome layer can be expressed as

$$G^H_{z\varphi}(\vec{r_1},\vec{r_1'}) = G^H_o(\vec{r_1},\vec{r_1'}) + G^{sc,H}(\vec{r_1},\vec{r_1'}) \ . \tag{5.32}$$

Here, G^H_o is the free space Green's function for the z-directed magnetic field created by the line source located at the position (r_1', φ_1') and carrying a φ_1-directed current,

$$G^H_o(\vec{r_1},\vec{r_1'}) = \frac{\partial}{\partial r_1'} G_o(\vec{r_1},\vec{r_1'}) = \sum_{n=-\infty}^{\infty} g^H_{on} \epsilon^{in\varphi_1} \ , \qquad r > r' \tag{5.33}$$

where $G_o(\vec{r_1},\vec{r_1'}) = \frac{i}{4} H^{(1)}_o(k|\vec{r_1} - \vec{r_1'}|)$ is the 2D free space scalar Green's function. The expansion coefficient is given as

$$g^H_{on} = \frac{i}{4} J_n'(k_o r_1') H_n^{(1)}(k_o r_1) e^{-in\varphi_1'} \tag{5.34}$$

The scattered part of the Green's function is written in terms of the coordinate system O as follows

$$G^{sc,H}(\vec{r},\vec{r'}) = \sum_{n=-\infty}^{\infty} -\frac{i}{4} K^H_n \frac{\partial}{\partial r_1'} (J_n(k_o r') J_n(k_o r) e^{-in(\varphi - \varphi')}) \ , \qquad r < c \ . \tag{5.35}$$

Then the function written in terms of the coordinate system O must be transformed into the coordinate system O_1, since the integral equation (5.28) is written in terms of O_1 system. Transformation is performed according to the following equation [34]

$$Z_n(k_o r) e^{in\varphi} = \sum_{p=-\infty}^{\infty} J_{p-n}(k_o L) Z_p(k_o r_1) e^{ip\varphi_1}, \qquad |r_1| > L \ . \tag{5.36}$$

where Z_n represents any kind of Bessel functions. By the application of the equation (5.36), the scattered part of the Green's function became

$$G^{sc,H}(\vec{r_1},\vec{r_1'}) =$$
$$-\frac{i}{4} \sum_{n=-\infty}^{\infty} K^H_n \sum_{p=-\infty}^{\infty} J_{p-n}(k_o L) J_p'(k_o r_1') e^{-ip\varphi_1'} \sum_{l=-\infty}^{\infty} J_{l-n}(k_o L) J_l(k_o r_1) e^{il\varphi_1} . \tag{5.37}$$

The restrictions in (5.35) and (5.36) yield some limitations on L, which are given as $L < a$ and $L < c$. Substituting the Green's function and surface current density in the series form into the integral equation (5.28), dual series equations are obtained as

$$\sum_{n=-\infty}^{\infty} x^H_n J_n'(k_o a) H_n^{(1)'}(k_o a) e^{in\varphi_1} - \sum_{n=-\infty}^{\infty} J_n'(k_o a) Y_n \epsilon^{in\varphi_1} =$$
$$- \sum_{n=-\infty}^{\infty} b^H_n e^{in\varphi_1} \ , \qquad \varphi_1 \in M \tag{5.38}$$

$$\sum_{n=-\infty}^{\infty} x_n^H e^{in\varphi_1} = 0 \ , \qquad \varphi_1 \in S \tag{5.39}$$

where

$$Y_n = \sum_{m=-\infty}^{\infty} x_m^H J_m'(k_o a) L_{mn} \tag{5.40}$$

and

$$L_{mn} = \sum_{q=-\infty}^{\infty} K_q^H J_{m-q}(k_o L) J_{n-q}(k_o L) \ . \tag{5.41}$$

DSE's are then converted to a certain canonical form and regularized by RHP technique. The problem is reduced to an infinite matrix equation for the unknown Fourier coefficients as follows

$$(I - A^o + A)x = B \tag{5.42}$$

where

$$A_{ln}^o = \Delta_n^H T_{ln}^H \tag{5.43}$$

$$A_{ln} = i\pi(k_o a)^2 J_n'(k_o a) G_{ln} \tag{5.44}$$

and

$$G_{ln} = \sum_{u=-\infty}^{\infty} J_u'(k_o a) L_{nu} T_{lu}^H \ . \tag{5.45}$$

Furthermore, B matrix is given as

$$B_l = i\pi(k_o a)^2 \sum_{n=-\infty}^{\infty} b_n^H T_{ln}^H \ . \tag{5.46}$$

Since its operator is compact in the Hilbert space l^2[8], the truncation of the infinite matrix equation yields the solution with any desired accuracy. The resultant algebraic equation is Fredholm second kind. Therefore, the Fredholm theorems state that the solution exists and unique.

In the far field, the radiation pattern is given as

$$\phi(\varphi) = \sum_{n=-\infty}^{\infty} (-i)^n \Big(\sum_{m=-\infty}^{\infty} (x_m^H J_m'(k_o a) + J_m(k_o r_{s1}) e^{-im\theta_s}) J_{m-n}(k_o L) \Big) M_n^H N_n^H e^{in\varphi} \tag{5.47}$$

where M_n^H and N_n^H are explained in equations (5.26) and (5.27).

Chapter 6

NUMERICAL RESULTS

In this section, the normalized radiation patterns of some reflector antennas in free space and inside a circular dielectric radome are calculated. Various antenna dimensions, feeder parameters and radome geometries are considered, and some properties of the reflector antennas are discussed through the results obtained. Besides, the results are compared with the solutions found by the physical optics method and the method of moments.

Although the explained regularization procedure was equally efficient for any angular width $2\theta_{ap}$ and offset angle θ_0, we shall restrict the numerical analysis to the reflectors meeting the good approximation criterion $\Delta(\theta_{ap} + \theta_0) \leq 0.06\lambda$, as discussed in Section 3.

The computations in the reflector antenna in free space were performed by taking the matrix truncation number N_{tr} equal to the integer value of $(ka + 10)$ and the computations in the reflector antenna covered by a radome were performed by taking the matrix truncation number N_{tr} equal to the integer value of $(kd + 10)$ which guarantees an accuracy of 0.001 in calculating the far field. This is demonstrated in Figure 6.1 by the behavior of truncation error $\epsilon_x = max|x_n^{N_{tr}+1} - x_n^{N_{tr}}|/max|x_n^{N_{tr}}|$ as a function of the matrix order N_{tr}. Note that such a test is also useful for debugging a computer program. In addition to accuracy, computation time is another measure of efficiency in a numerical method. Figure 6.2 presents the computation times for different aperture dimensions. The results are from a SUN SPARCStation 2. Thus, 10 min. of CPU operation here, for a 20-λ scatterer, is not a long time compared to 0.5 min. of the CRAY X-MP supercomputer for a MoM-based solution, as was reported in [4]. According to [16], a CRAY X-MP can operate 50 to 200 times faster than this workstation.

For the validation of the results, we have checked the CSP solution in the limiting case corresponding to the real source point excitation. Further, in Figure 6.3, the high frequency solution of Suedan and Jull [2] (synthesized from AI and uniform GTD results for a CSP as front feeder) is compared with our circular reflector patterns for $D = 10\lambda$.

To obtain better agreement in the regions at the back of the reflector, the edge tangents of the parabolic and circular reflectors are equalized by adjusting the angular width of the circular reflector. For this geometry, the electrical error is 0.0011λ and the deviation between two patterns is smaller than $1\,dB$.

6.1 Reflector in free space

Figures 6.4 and 6.5 demonstrate the comparison of E and H-polarization cases, for front-fed and offset reflector antennas, respectively, having the aperture of $D \approx 10\lambda$ and $-10\,dB$ edge illumination. It is seen that the rear sidelobe levels are higher in H-polarization. This is expected since the edge effects are stronger due to transversal flow of the surface current. In Figure 6.5, there is also a few degrees shift at the main beam location of the offset antenna due to a non-symmetrical excitation and a circular aberration.

Furthermore, Physical Optics (PO) and method of moments radiation patterns are compared by our results for both polarizations. PO solution is performed for a complex position line source. The results are shown in Figures 6.6 and 6.7 for E and H polarization cases respectively. They are almost matched for the main beam and nearest sidelobes. PO solution follows the actual pattern better then the Aperture Integration (AI) result given in [2]. In addition, the deviation of the PO pattern is greater for H-Polarization case. This is an expected result because the edge effects are higher for H-Polarization. Figures 6.8 and 6.9 show the method of moments results.

The illumination of the circular offset reflector antenna by a beam field causes a wide and asymmetrical main beam especially for increasing beam aiming angles (see Figure 6.10). It is because the circular aberration for 2-D case increases by the greater deviation of the upper part of the reflector from the parabola. This kind of antennas have some application areas in airborne and navigational radar systems. In addition, PO radiation pattern is compared by present solution for the beam aiming angle of 48.475°. This is shown in Figure 6.11, the aperture dimension (D) 40λ, F/D_p=0.3 and h/D=0.125.

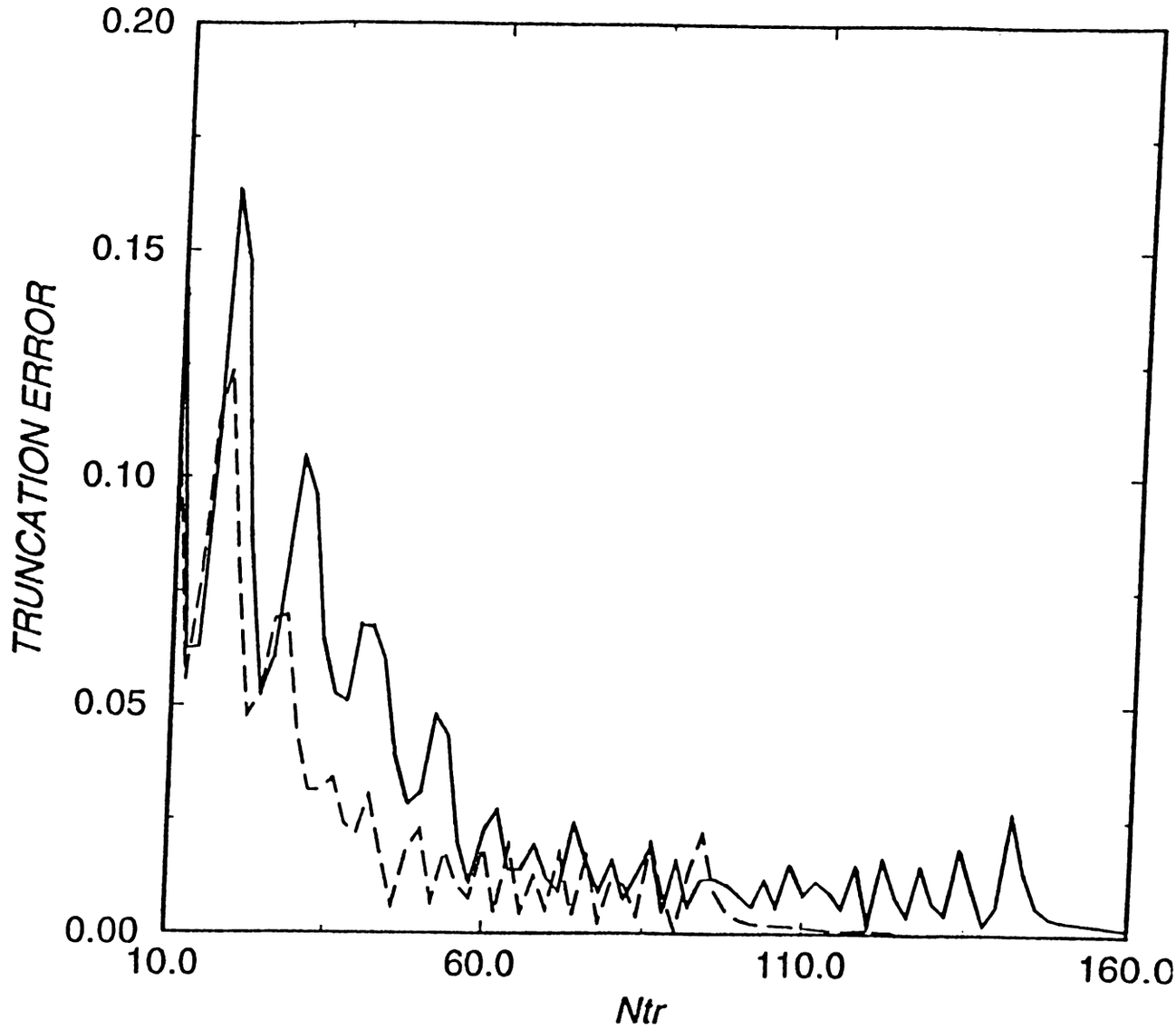

Figure 6.1: Truncation error dependence on the matrix order, for two sample geometries: ka=100(dashed curve) and ka=150 (solid curve), θ_o=0, θ_{ap}=30°, kb=9.

TABLE I
CPU TIMES OF THE COMPUTER CODES

$ka = 62.8, \theta_{ap} = 30°$	E-POL	H-POL
$D = 10\lambda, N_{tr} = 70$	2 min 55 sec	3 min 14 sec
$D = 20\lambda, N_{tr} = 130$	9 min 28 sec	10 min 8 sec
$D = 30\lambda, N_{tr} = 195$	22 min 6 sec	23 min 48 sec

Figure 6.2: CPU times for both polarizations.

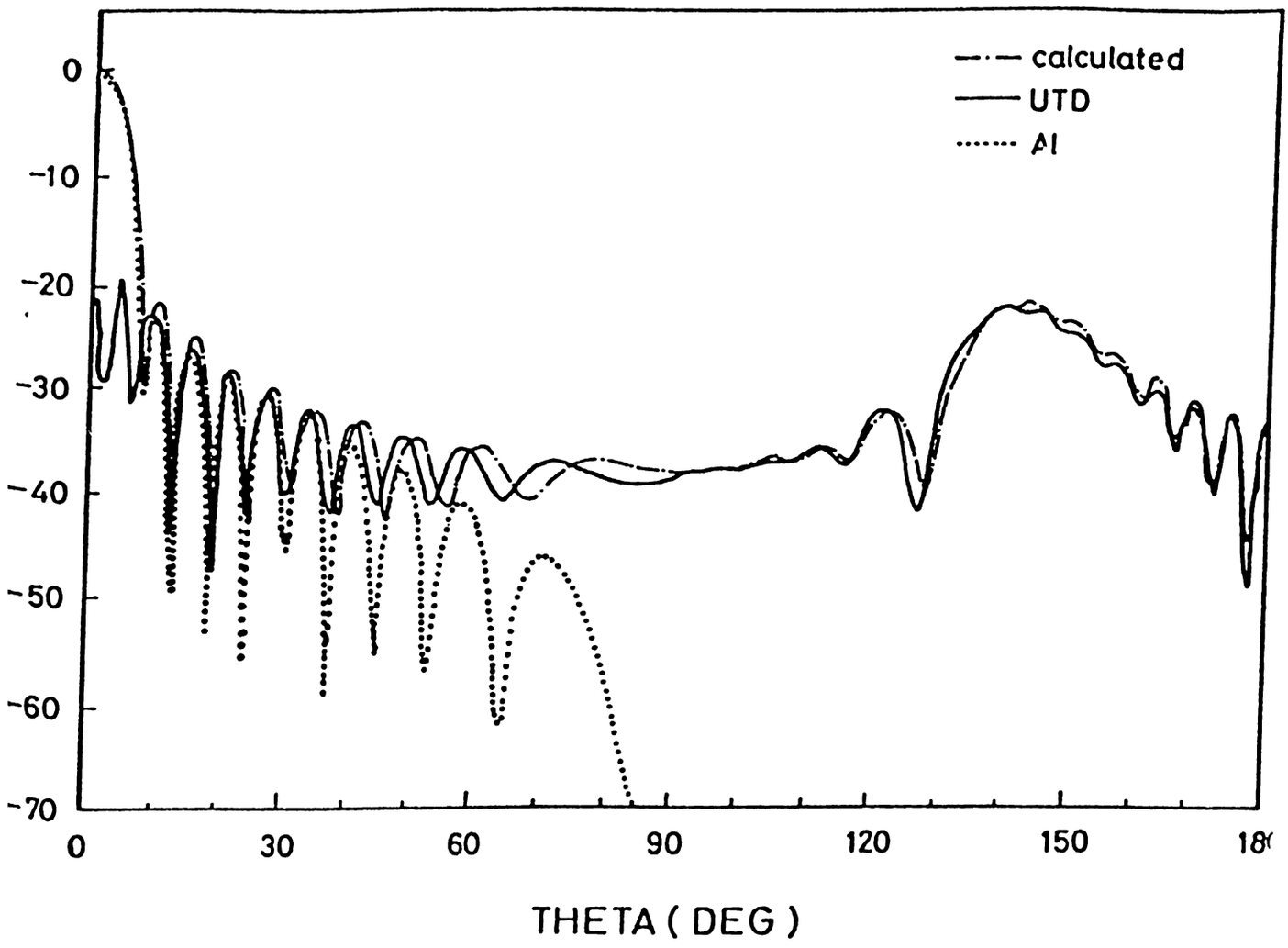

Figure 6.3: Comparison of E-Polarization radiation pattern of a parabolic reflector [2] (F/D=0.96, D=10λ) with a circular one (ka=120.57, $\theta_a p$=15°). Feed directivity parameter, kb=9.06 corresponds to a $-10.09\,dB$ edge illumination.

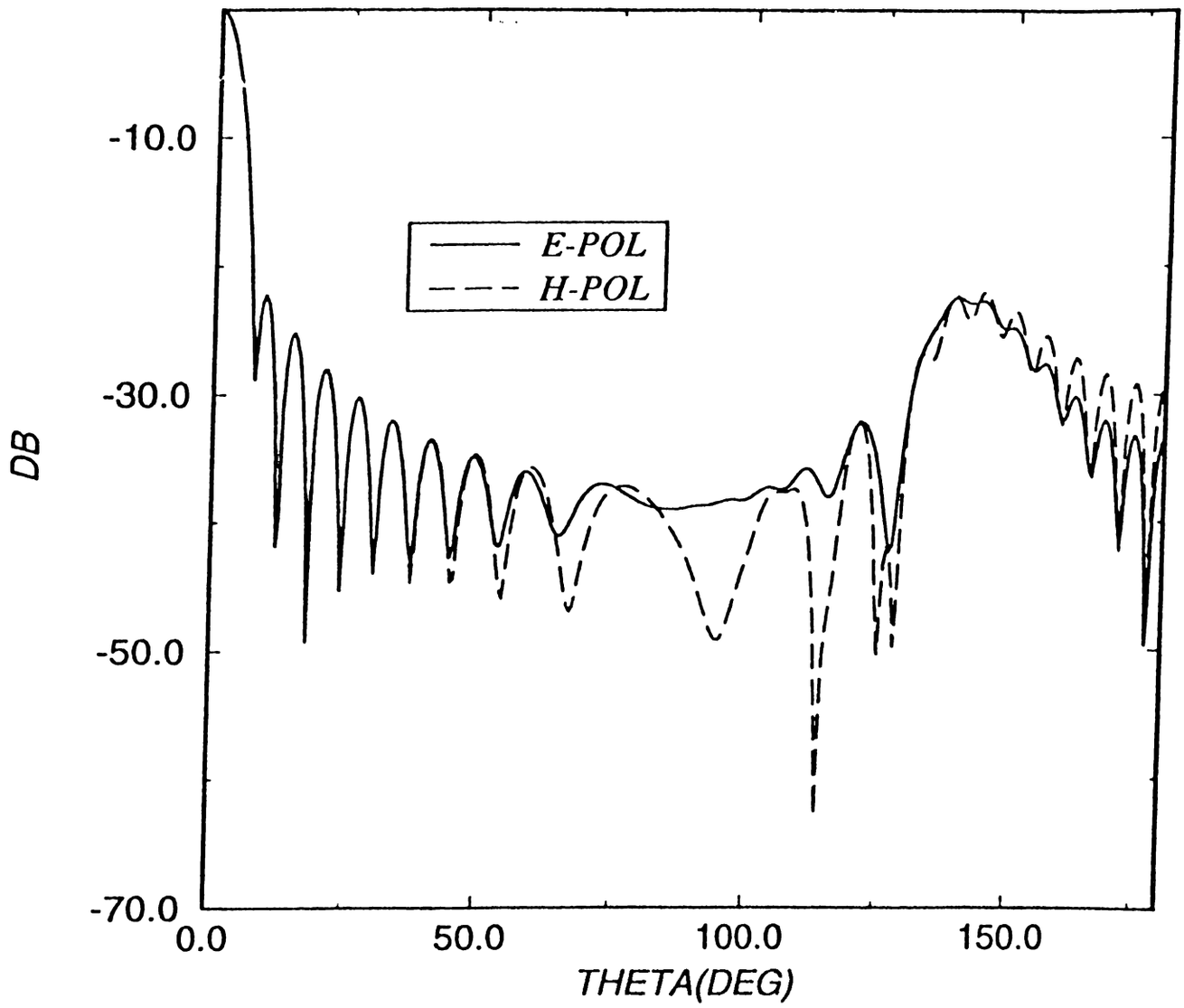

Figure 6.4: Comparison of E and H polarization radiation patterns for a front-fed symmetrical circular reflector of ka=120.57, $\theta_{ap} = 15^o$ where D=10λ and $\theta_o = \beta = 0^o$. Feed parameters are kr_o=60.28, kb=9.06($-10.09\,dB$ edge illumination).

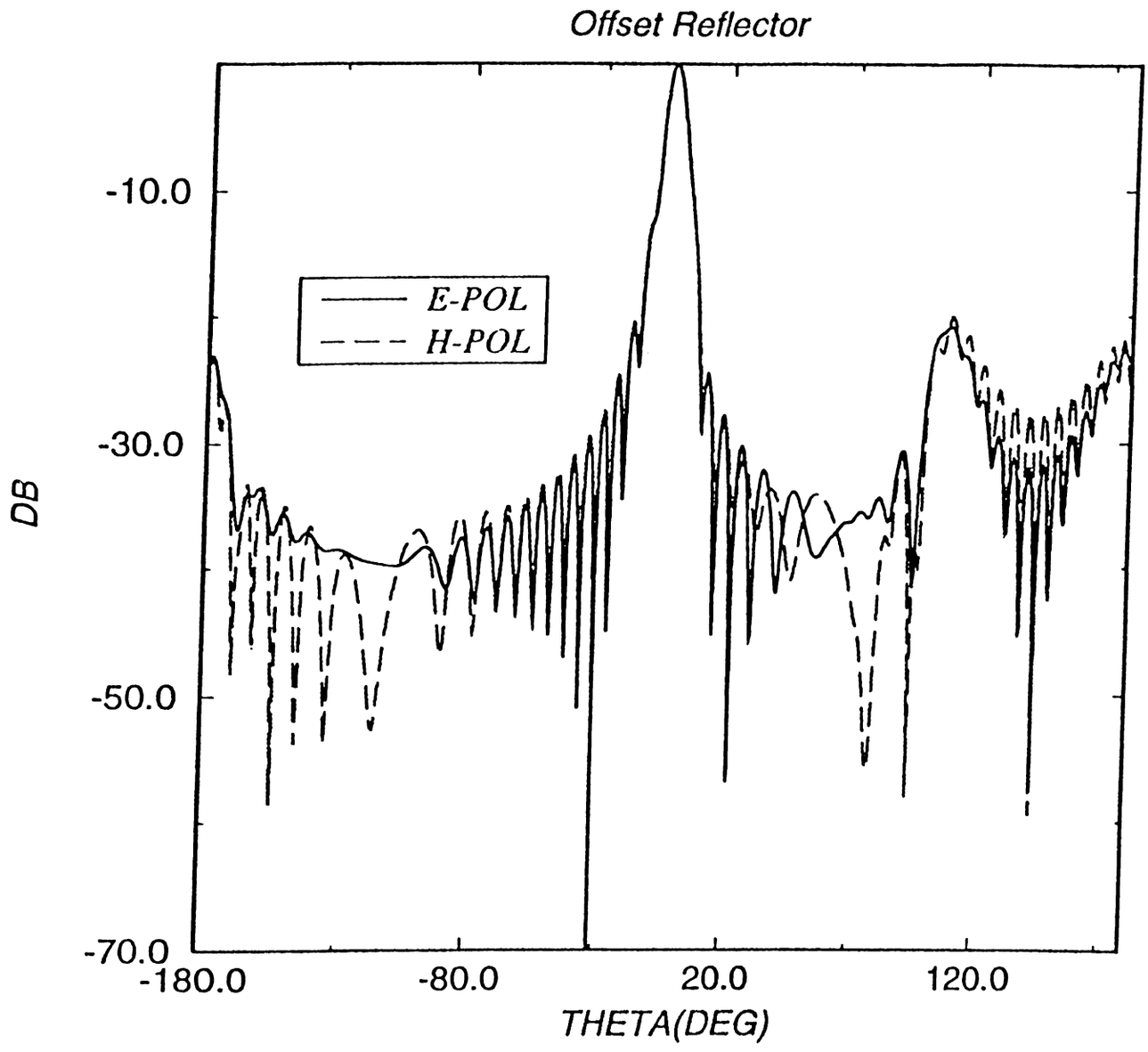

Figure 6.5: Comparison of E and H polarization radiation patterns for a offset circular reflector of ka=120.57, $\theta_{ap} = 15.91°$, $\theta_o = 22°$ where $D = 9.77\lambda$. Feed parameters are $kr_o = 60.28$, feed beaming angle $\beta = 39°$ and kb=11.05 corresponds to a $-9.78\,dB$ and $-10.14\,dB$ edge illuminations for lower and upper edges.

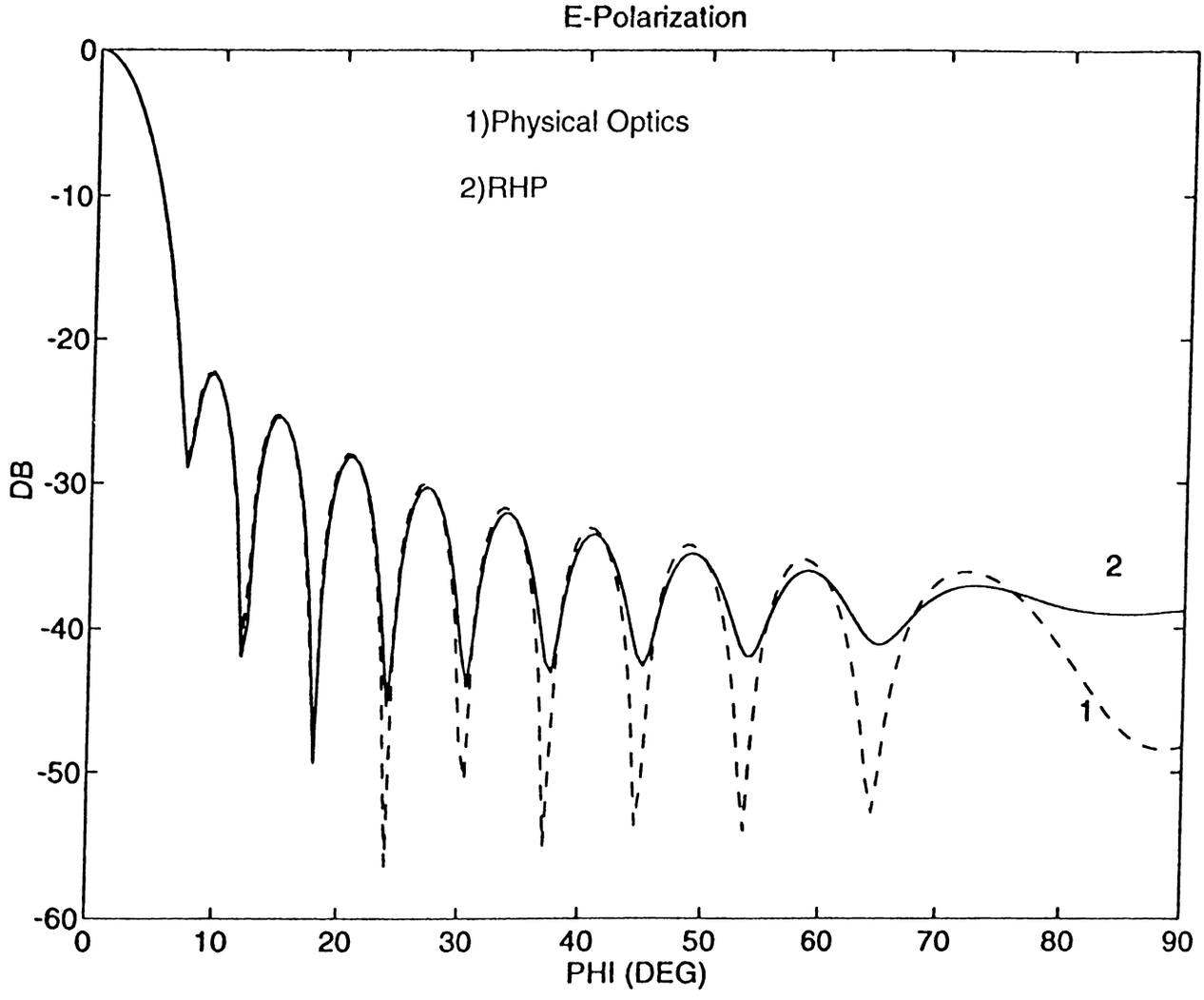

Figure 6.6: Comparison of the physical optics radiation patterns with the present solution for a front-fed symmetrical circular reflector of ka=120.57, $\theta_{ap} = 15°$(D=10λ). Feed parameters are kr_o=60.28, kb=9.06($-10.09\,dB$ edge illumination): E-Polarization case.

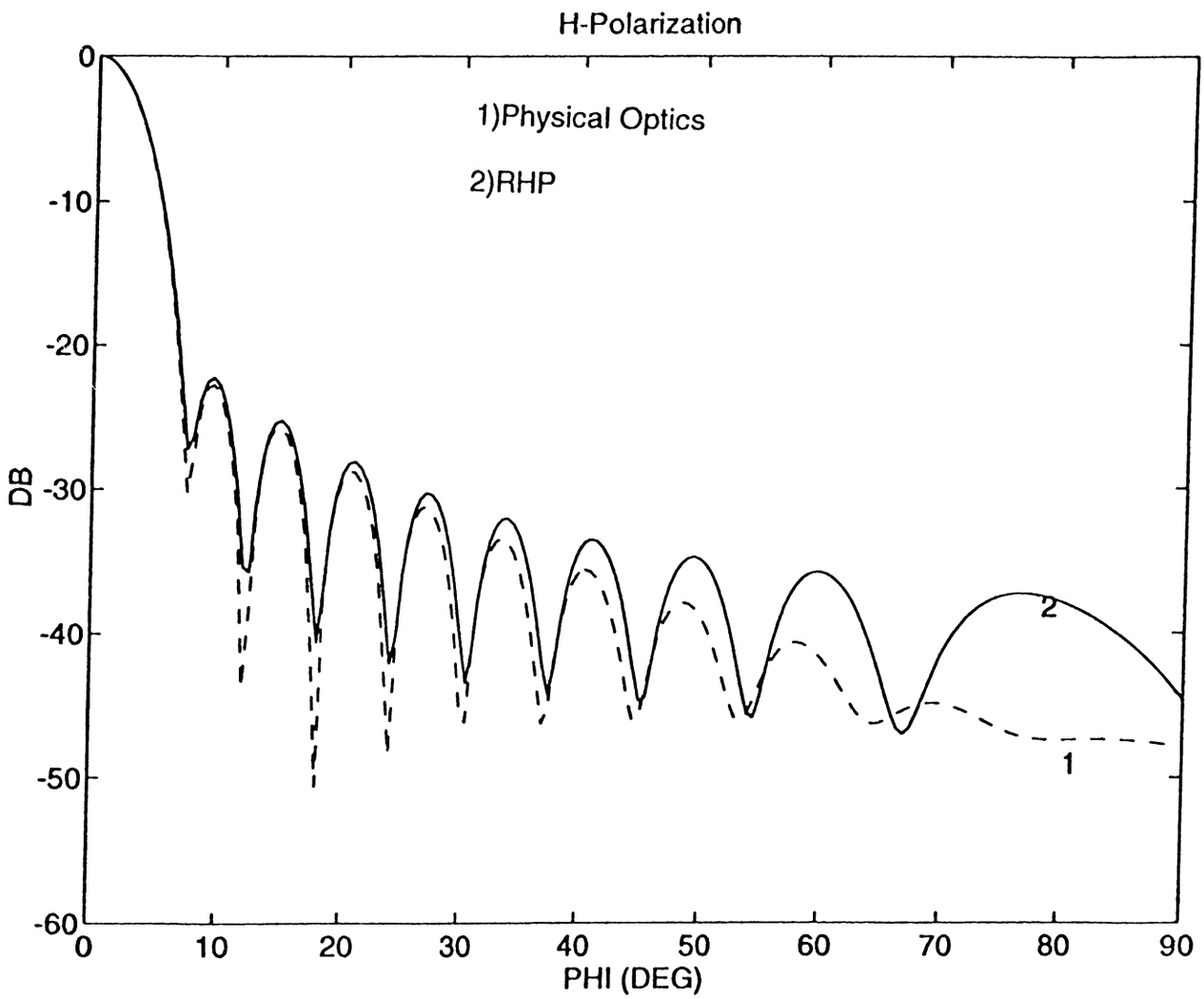

Figure 6.7: Comparison of the physical optics radiation patterns with the present solution for the same geometry as in Figure 6.6: H-Polarization case.

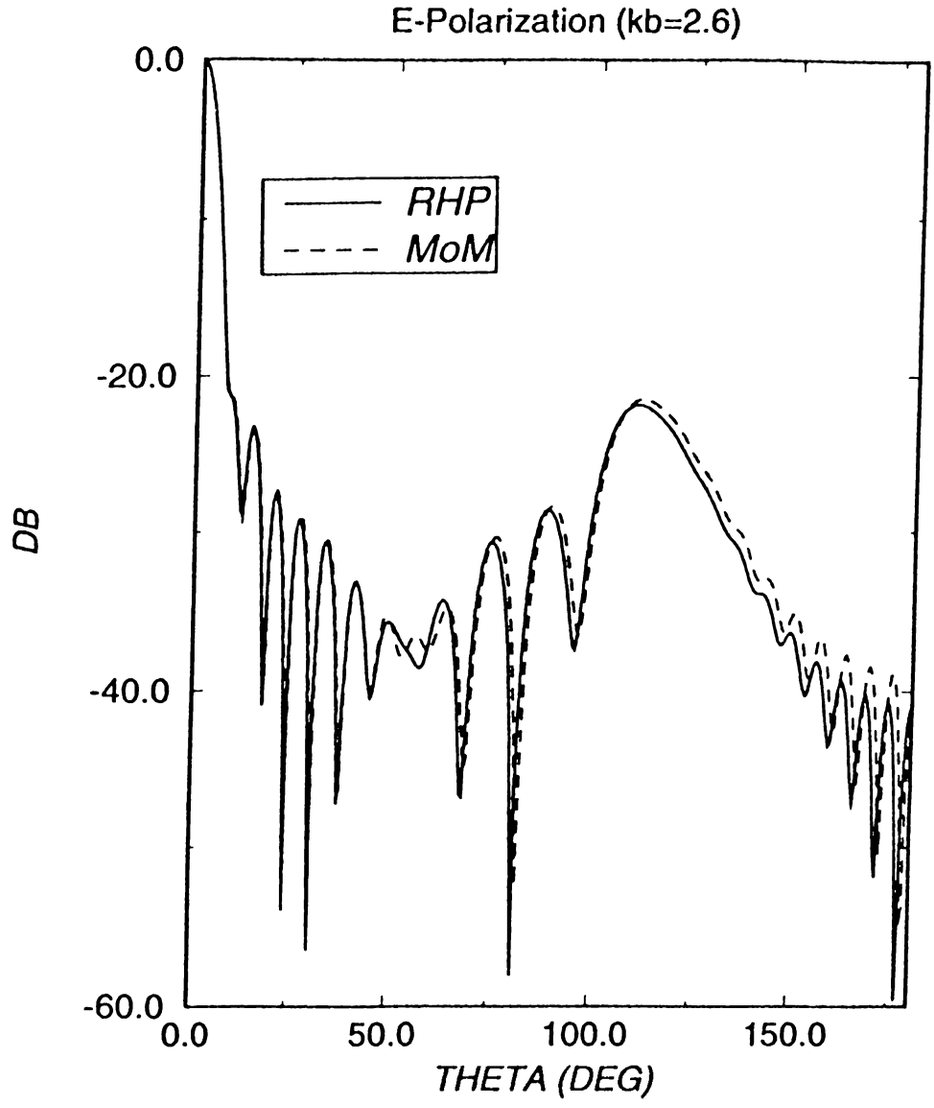

Figure 6.8: Comparison of method of moments solution with the method of regularization result for E polarization case. Front-fed symmetrical circular reflector of ka=62.8, $\theta_a p = 29.74^o (D = 10\lambda)$. Feed parameters are kro=31.4 and kb=2.6 (-9 dB edge illumination).

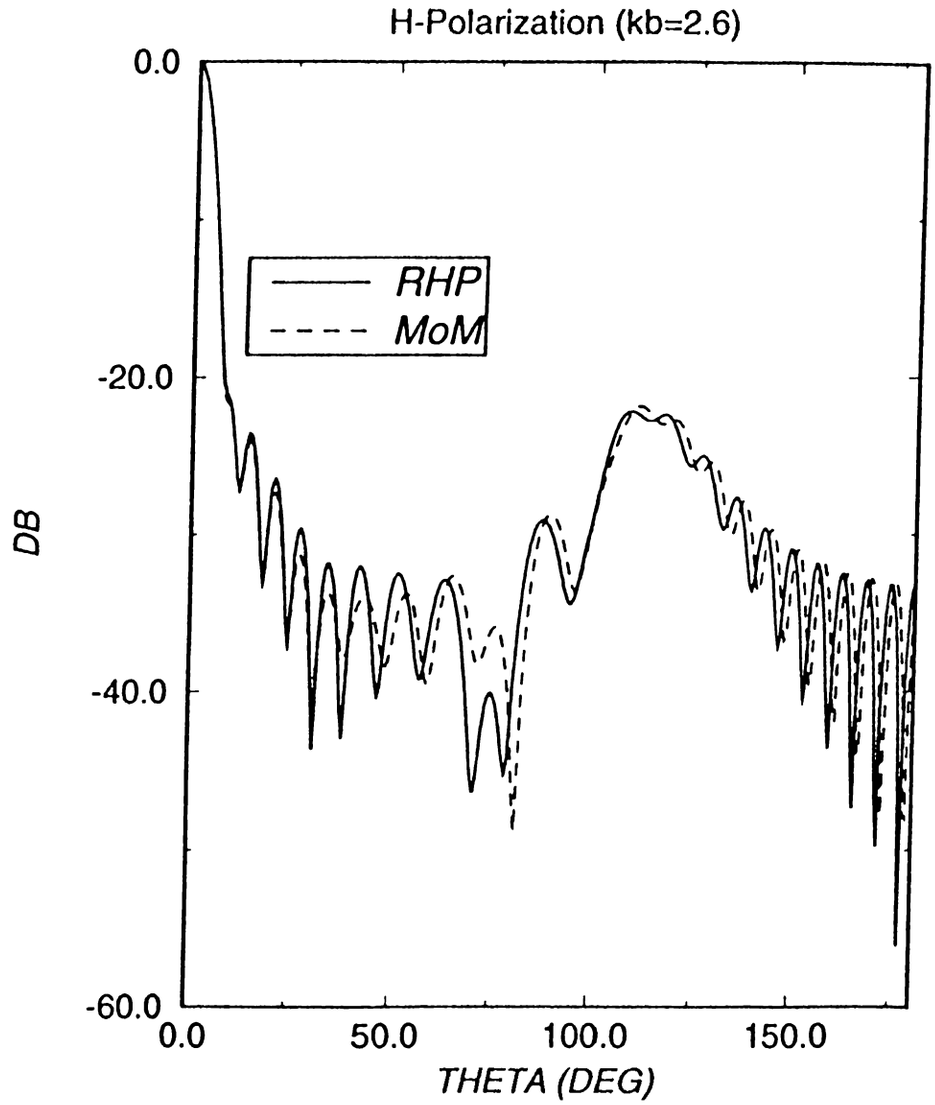

Figure 6.9: Comparison of method of moments solution with the method of regularization result for H polarization case for the previous geometry

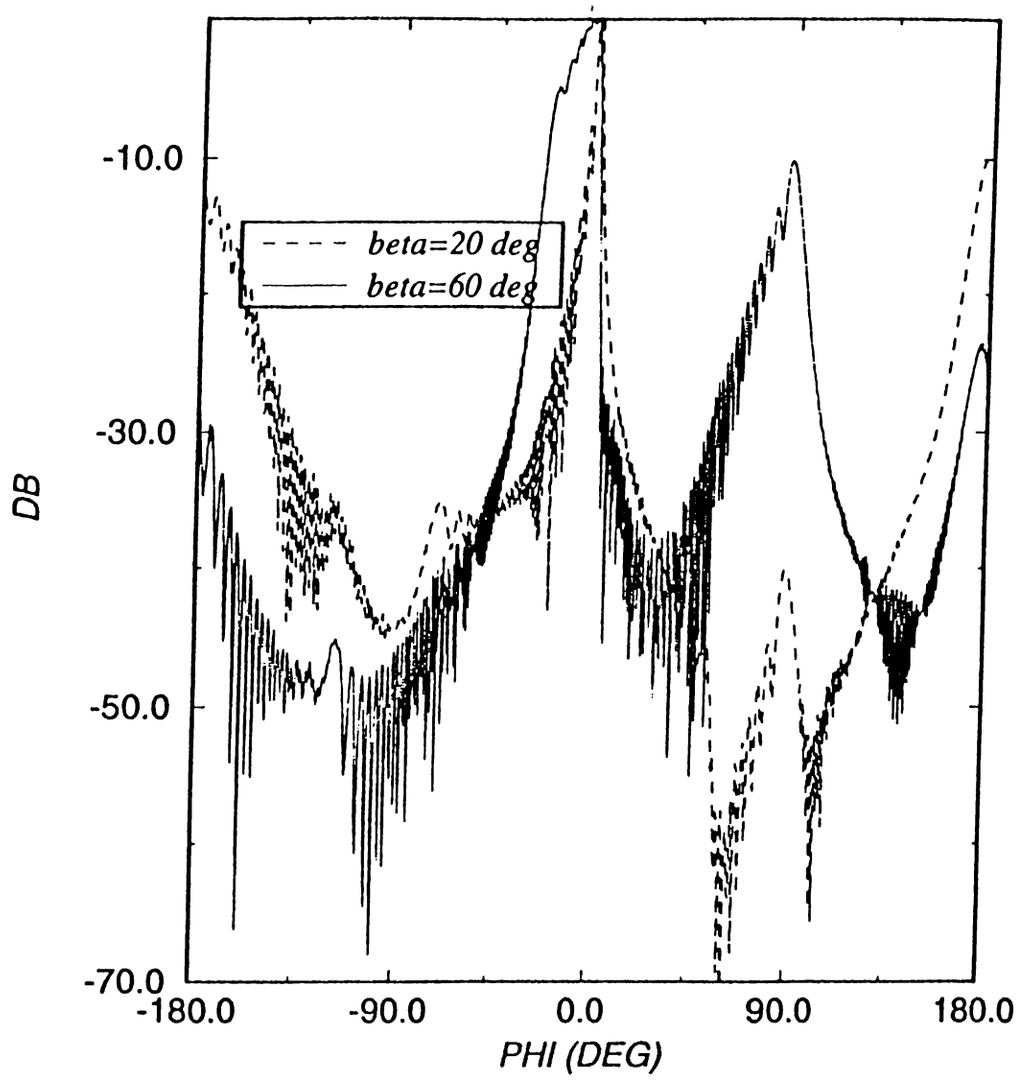

Figure 6.10: Radiation patterns of large circular offset reflector for $F/D_P = 0.3$, h/D=0.125 and $D = 50\lambda$ where $\theta_{ap} = 25.56^o$ and $\theta_o = 30.87^o$. Feed taper is defined with the source directivity parameter kb=5.46 corresponding to $-10\,dB$ for a half angle ψ_S of 37.895°.

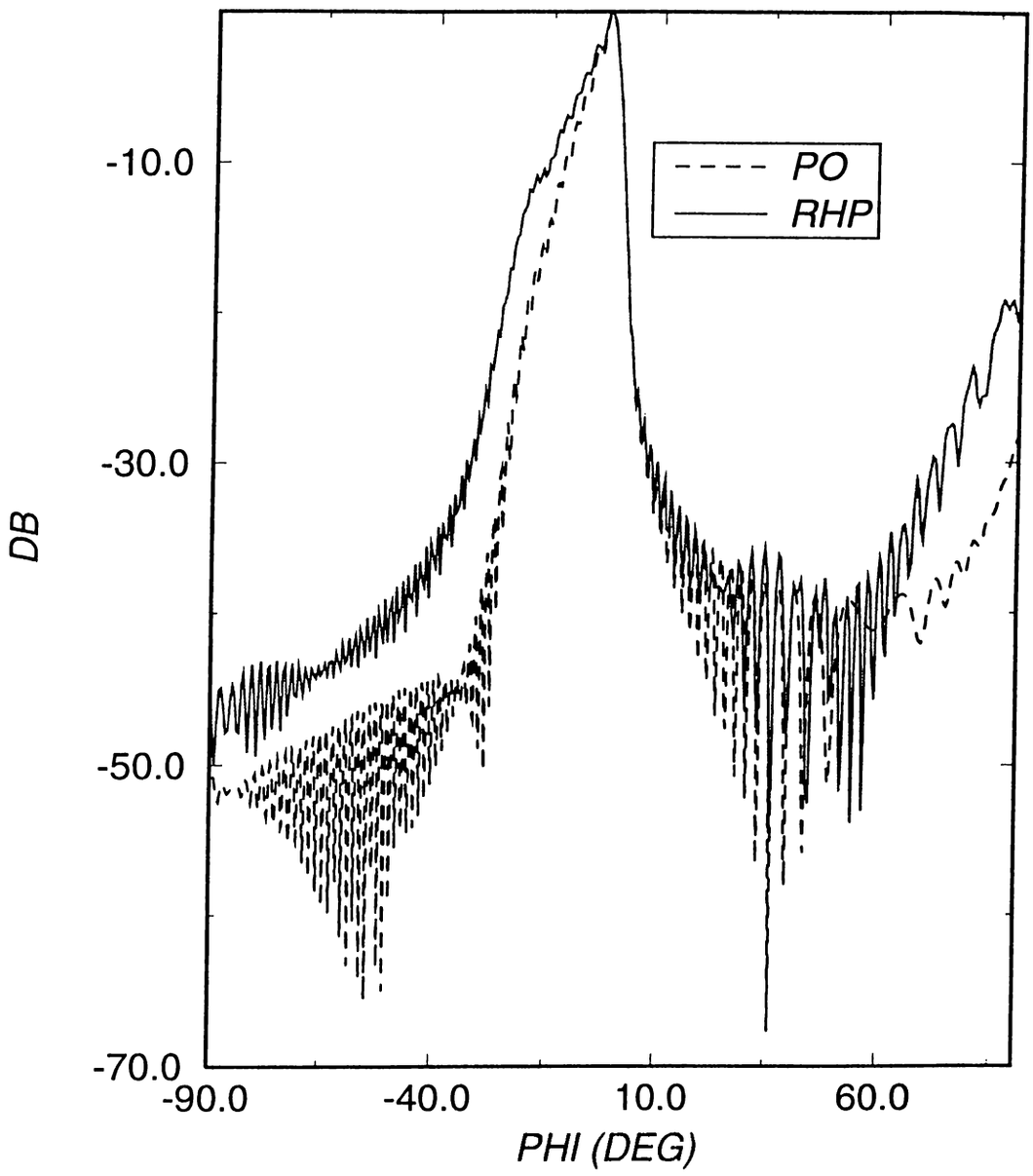

Figure 6.11: Radiation pattern comparison of PO and RHP for the beam aiming angle of 48.475° with the source directivity parameter kb=5.46 for a $-10\,dB$ half angle edge illumination.

6.2 Directivity and radiated power

In this section, the directivity and the total radiating power effects are considered. The effect of the source directivity for both E and H-polarizations is examined in Figures 6.12 and 6.13, for a $D = 10\lambda$ reflector. Source directivity is increased with increasing parameter kb and the results show that all the sidelobe levels are decreased while the main beam width changes little for constant electrical dimensions of the reflector. Figures 6.14 and 6.15 show the radiation patterns in E and H-polarization cases for two reflector dimensions, $D = 10\lambda$ and 20λ. It is seen that the main beam is narrower for a larger aperture and the sidelobe level is reduced, except for the spillover sidelobe which is the same due to the same edge illumination.

Figure 6.16 presents the plots of the ratio P/P_0 as the aperture dimension of the reflector increases. The variation of P/P_0 around unity is within 7% and caused by the in-phase or out-of-phase interference of the weak edge-diffracted field with a stronger reflected field. Besides, the oscillation levels are higher in H-polarization, because of the stronger edge effects. Figure 6.17 also shows the directivity variation for the same conditions. It is seen that there is a slightly oscillatory linear increase in the directivity for increasing aperture dimension D, for the same reason as above. Note that the primary feed directivity here is only $D_0 = 7.82$. As expected, increasing source directivity reduces the edge effects so that the variations in P/P_0 decrease rapidly (See Figure 6.18). For a practical case, the edge illumination can be taken as $9\,dB$ below the center of the reflector, then $P/P_0 = 1$ with 0.001 accuracy. Similarly, increasing the feed directivity increases the directive gain since the diffraction effect is reduced. Figure 6.19 presents also the variation of overall directivity D and the feed directivity D_o with kb.

The influence of the feed beam aiming angle on the directive gain (DG) and sidelobe level (SLL) was obtained and shown in Figure 6.20 and 6.21. A similar study was performed by W. Stutzman and M. Terada for the optimization of offset parabolic antenna design [27]. They are used an available computer code GRASP-7 [28] based on the PO approach, but the plot of DG is not in agreement with the SLL plot in [27]. DG variation as a function of beam aiming angle is shown in Figure 6.20, it is seen that the maximum value of DG shifts to the lower edge due to the increasing circular aberration towards the upper edge. Besides, DG decreases for too high and for too low beam aiming angles as the spillover radiation increases. In Figure 6.21, the level of the spillover lobe is given and the highest spillover shifts from the lower edge to the upper

edge as the beam aiming moves in the same direction.

6.3 Reflector inside a radome

Figures 6.22 and 6.23 represent the radiation patterns of a circular reflector with concentric dielectric radome for both E and H polarizations, respectively. In these plots, the two cases of different radome thicknesses t are compared with the case of the reflector without a radome. The wavelength in the figures is the wavelength in the radome material λ_d where $\lambda_d = 0.5\lambda$ when $\epsilon_r = 4$. It is seen that when the halfwavelength design of the radome walls are performed ($t = 0.5\lambda_d$), the transmission through the radome walls is optimized, therefore the radiation pattern can be obtained with a minimum distortion [25]. The distorted radiation patterns ($t = 0.44\lambda_d$) are almost in the same level for both E and H polarization cases. But the edge effects are higher for H-Polarization, so the backlobe levels appear at a higher level.

In the Figures 6.24 and 6.25, the effect of the decreasing edge illumination is presented. For both polarizations, the decreasing edge illumination increases the distortion in the radiation patterns for an unmatched radome. It can be thought as an effect of the main beam propagation through the circular dielectric shell.

The free space radiation patterns can be obtained for each case by converging the permitivity of the radome material (ϵ_r) to unity that gives a validation of the results.

Figure 6.26 shows the radiation pattern for the nonconcentric radome case. For the half-wavelength design, the pattern is almost the same as in the case of the reflector in free space (the shift is $kL = ka\cos(\theta_{ap})$). It is the fact since the reflections from the radome is minimized. But the plots for the thickness less then the halfwavelength do not coincide because of essential reflections from the radome.

Thus, summarizing the results presented in this Section, one can conclude that the RHP method gives a valuable opportunity to simulate all the considered and other properties of the 2-D reflector antennas (such as the focal shift [29], front-to-back ratio [30] and so on) in a mathematically rigorous manner, effectively, and with any desired numerical accuracy.

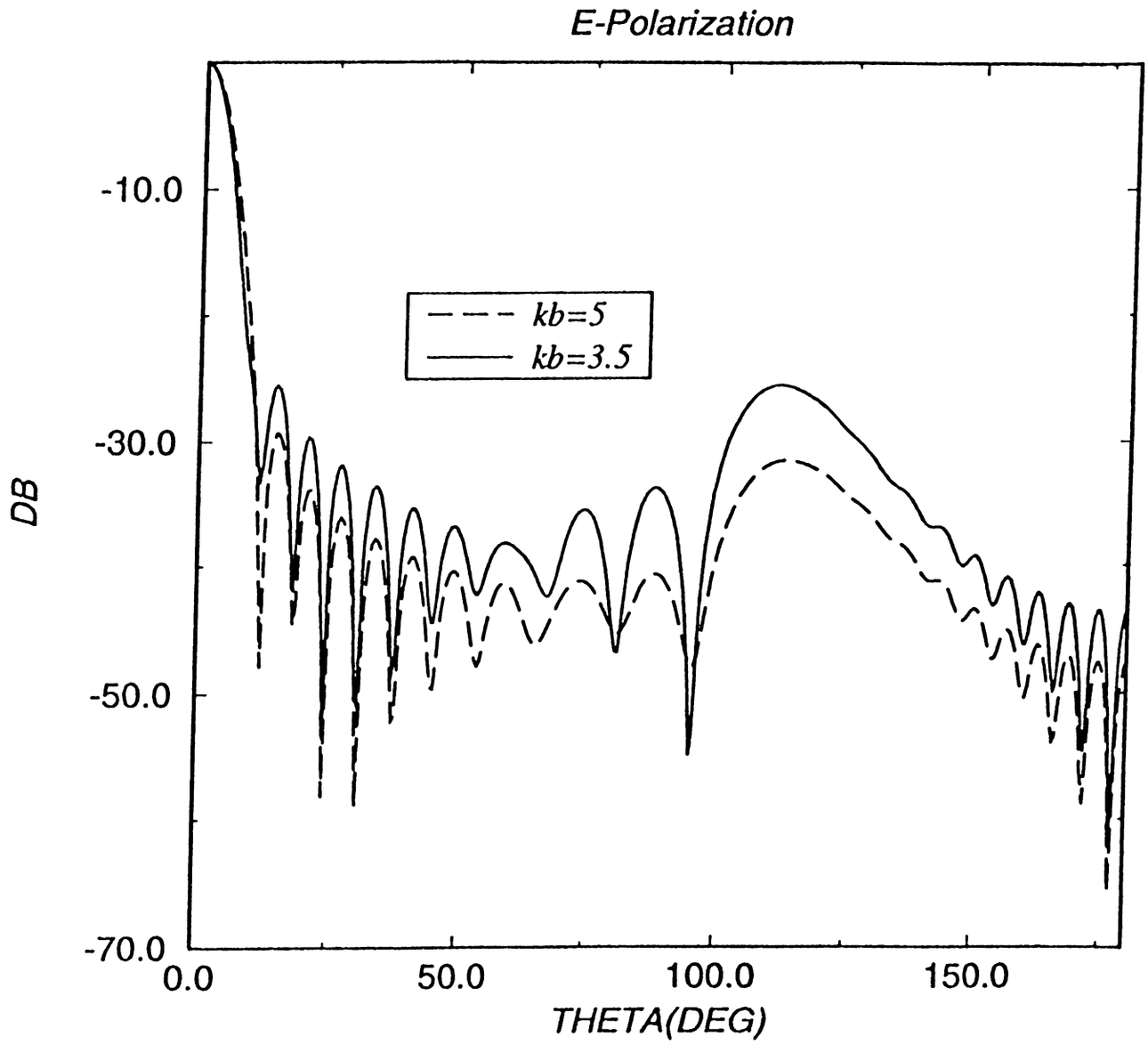

Figure 6.12: Effect of the different edge taperings for E-Polarization case for a front-fed symmetrical reflector with ka=62.8, θ_{ap} = 29.74° (D=9.92λ). Feed directivity parameters, kb=3.5 and kb=5 correspond to $-13.02\,dB$ and $-18.21\,dB$ edge illuminations.

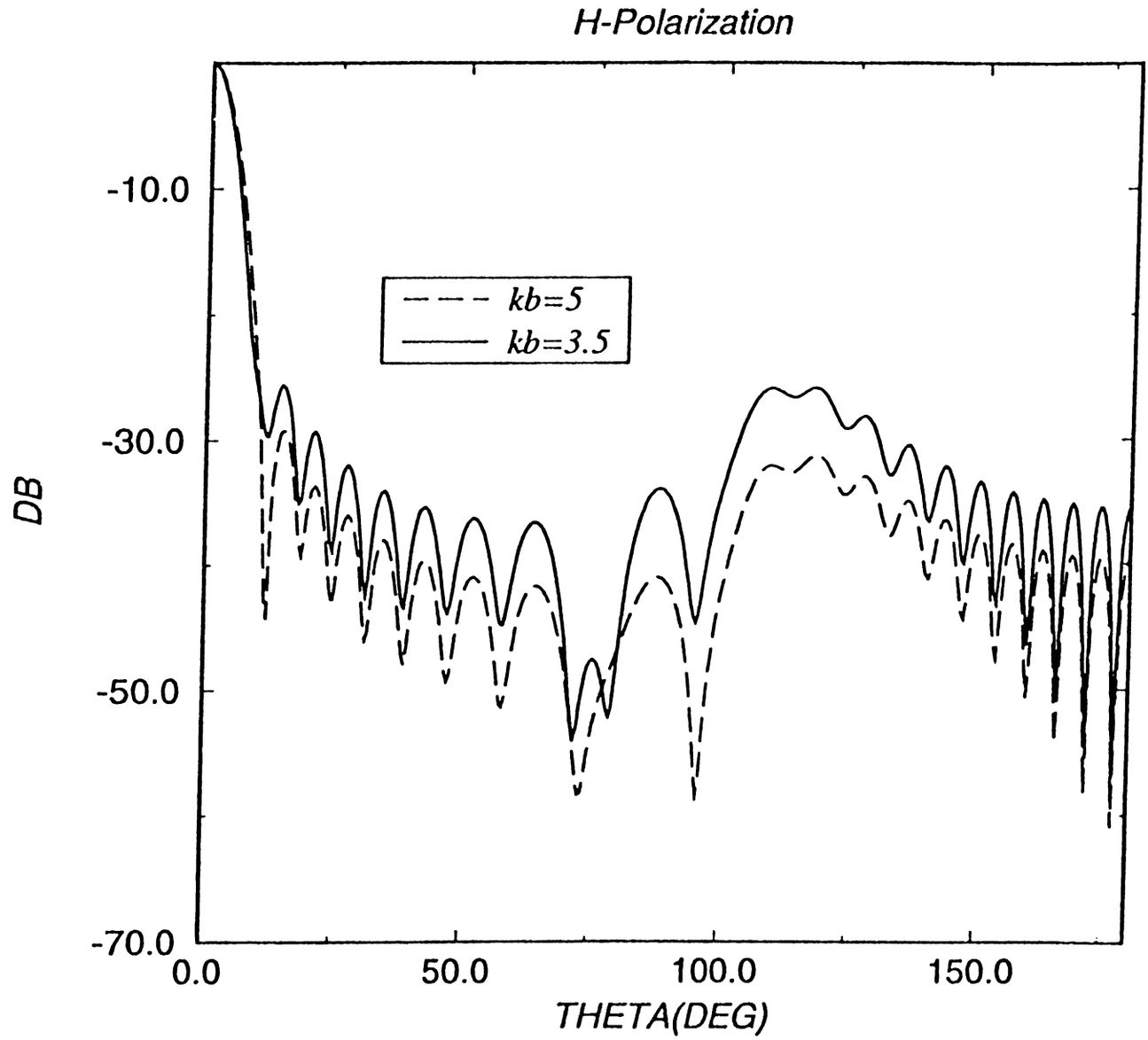

Figure 6.13: Effect of the different edge taperings for H-Polarization case for a front-fed symmetrical reflector with ka=62.8, θ_{ap} = 29.74° (D=9.92λ). Feed directivity parameters, kb=3.5 and kb=5 correspond to $-13.02\,dB$ and $-18.21\,dB$ edge illuminations.

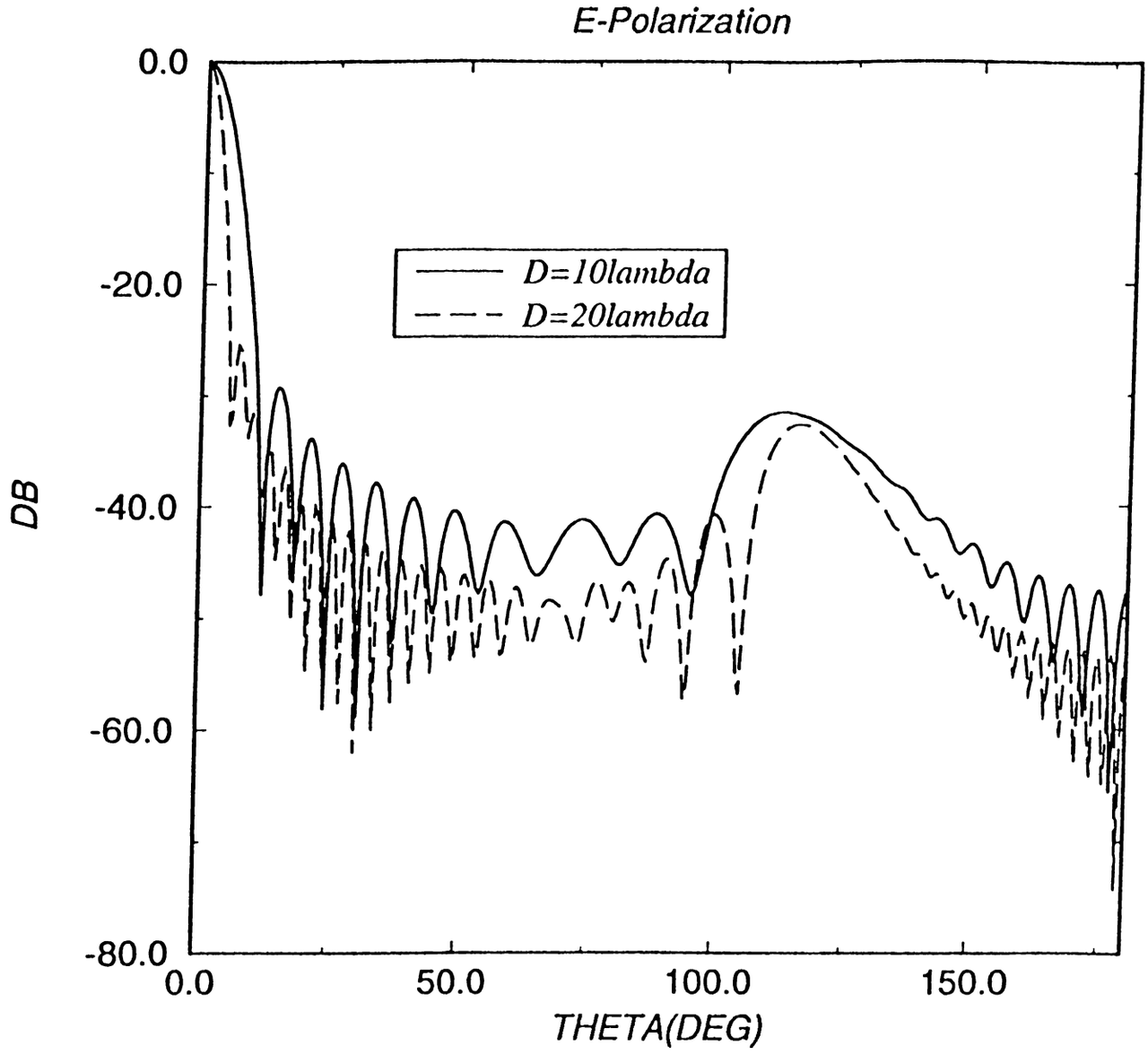

Figure 6.14: Effect of the different aperture dimensions for E-Polarization case for a front-fed symmetrical reflector of the constant angular halfwidth $\theta_{ap} = 29.74°$. Feed directivity parameter kb=5 provides $-18.21\ dB$ edge illumination.

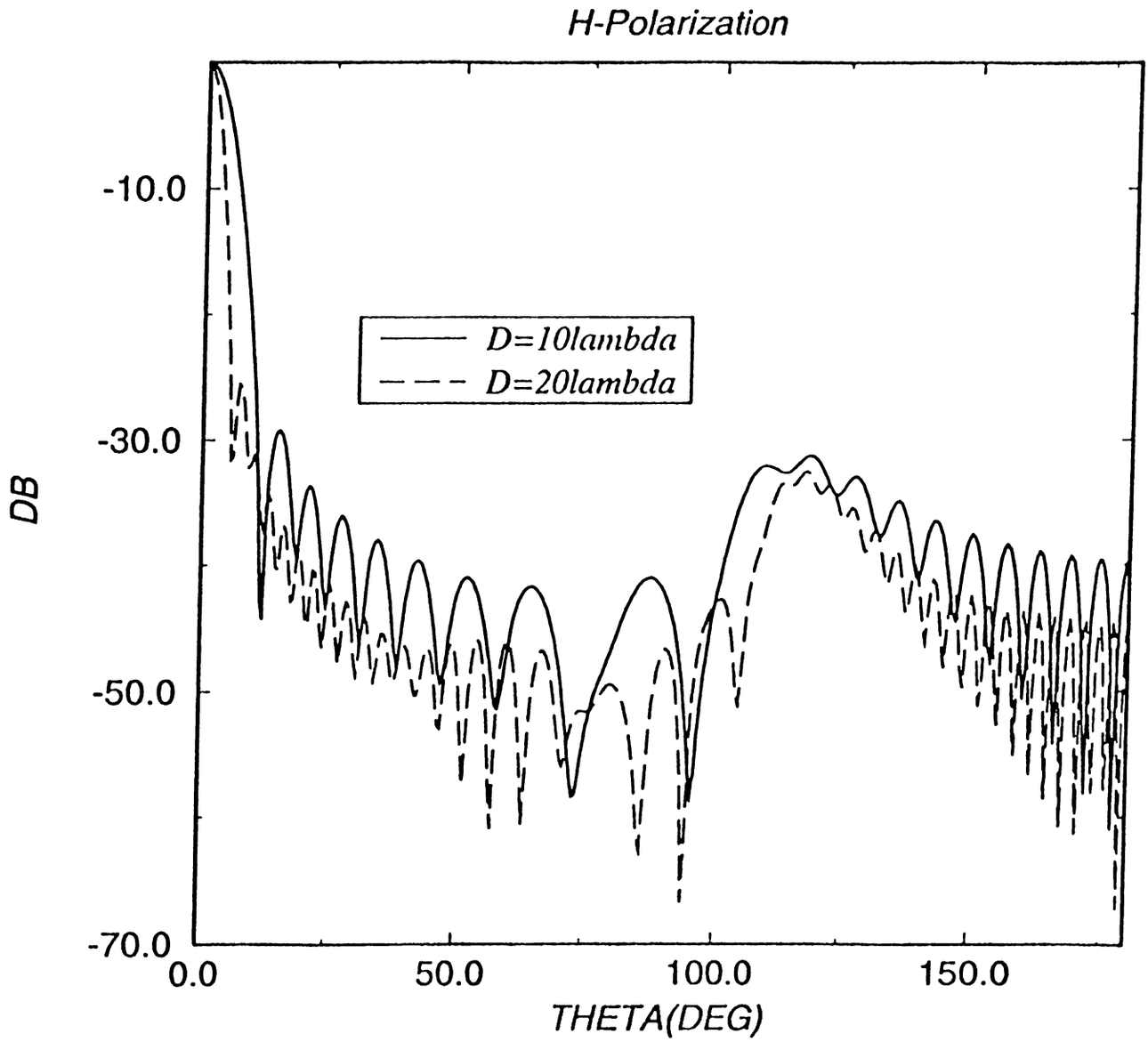

Figure 6.15: Effect of the different aperture dimensions for H-Polarization case for a front-fed symmetrical reflector of the constant angular halfwidth $\theta_{ap} = 29.74°$. Feed directivity parameter kb=5 provides $-18.21\,dB$ edge illumination.

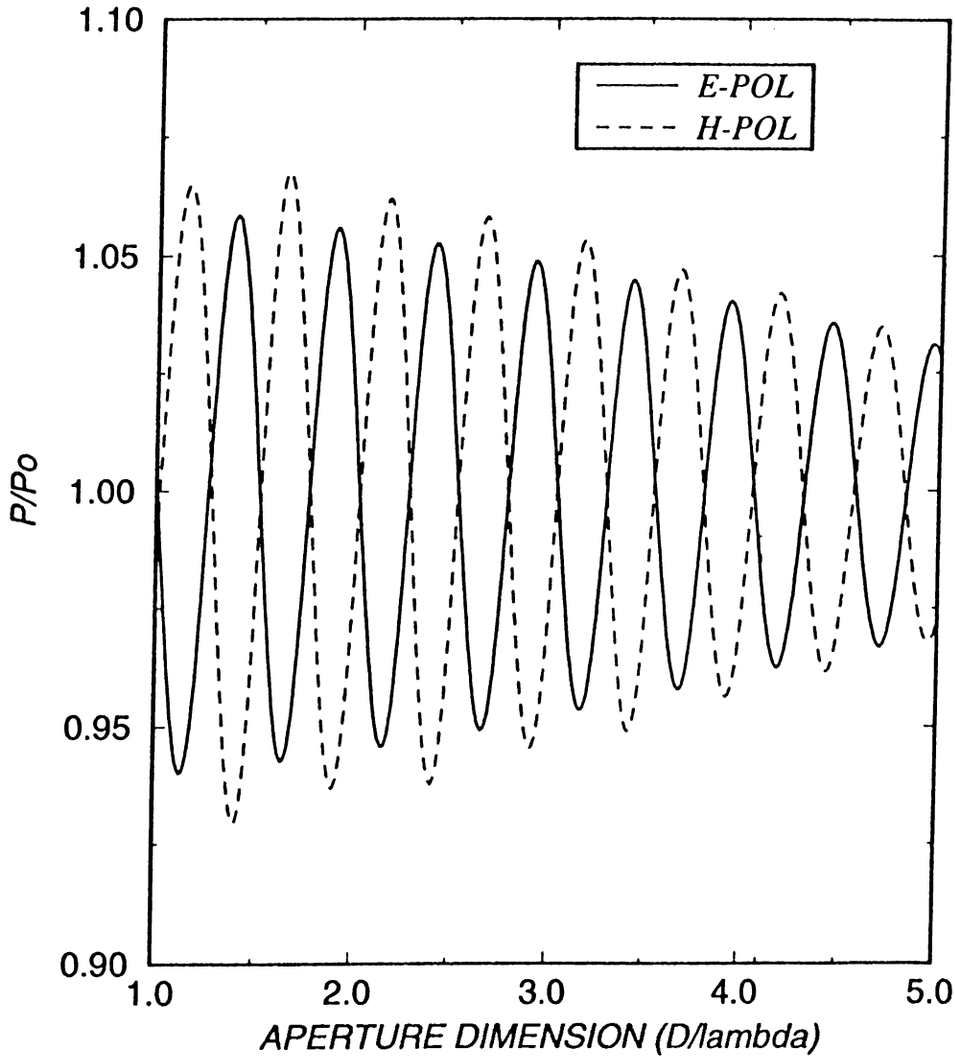

Figure 6.16: Total radiated power variation with increasing aperture dimension for a front-fed symmetrical reflector of $\theta_{ap} = 15°$ and f/D=0.96. Feed directivity parameter kb=1.5 corresponds to $-1.65\,dB$ edge illumination.

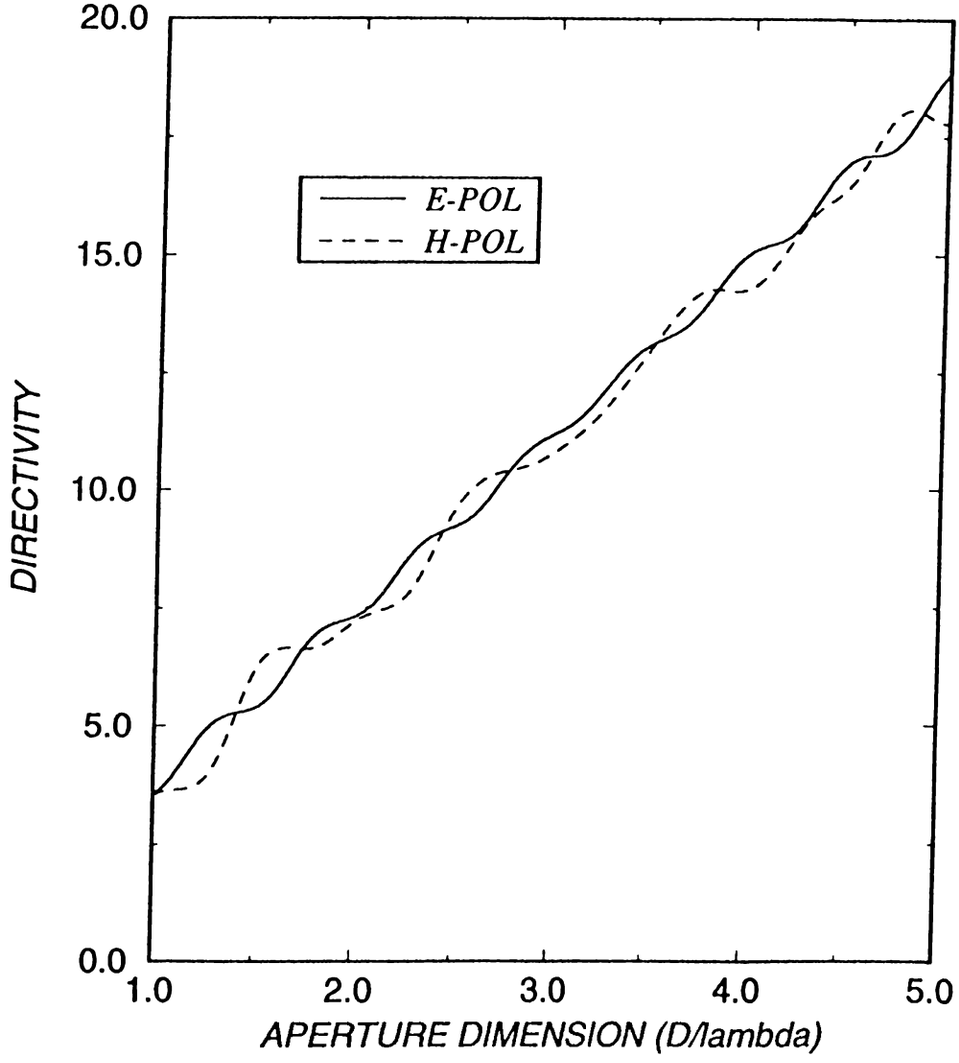

Figure 6.17: Directivity variation with increasing aperture dimension for a front-fed symmetrical circular reflector of $\theta_{ap} = 15^{o}$ and f/D=0.96. Feed directivity parameter kb=1.5 corresponds to $-1.65\,dB$ edge illumination.

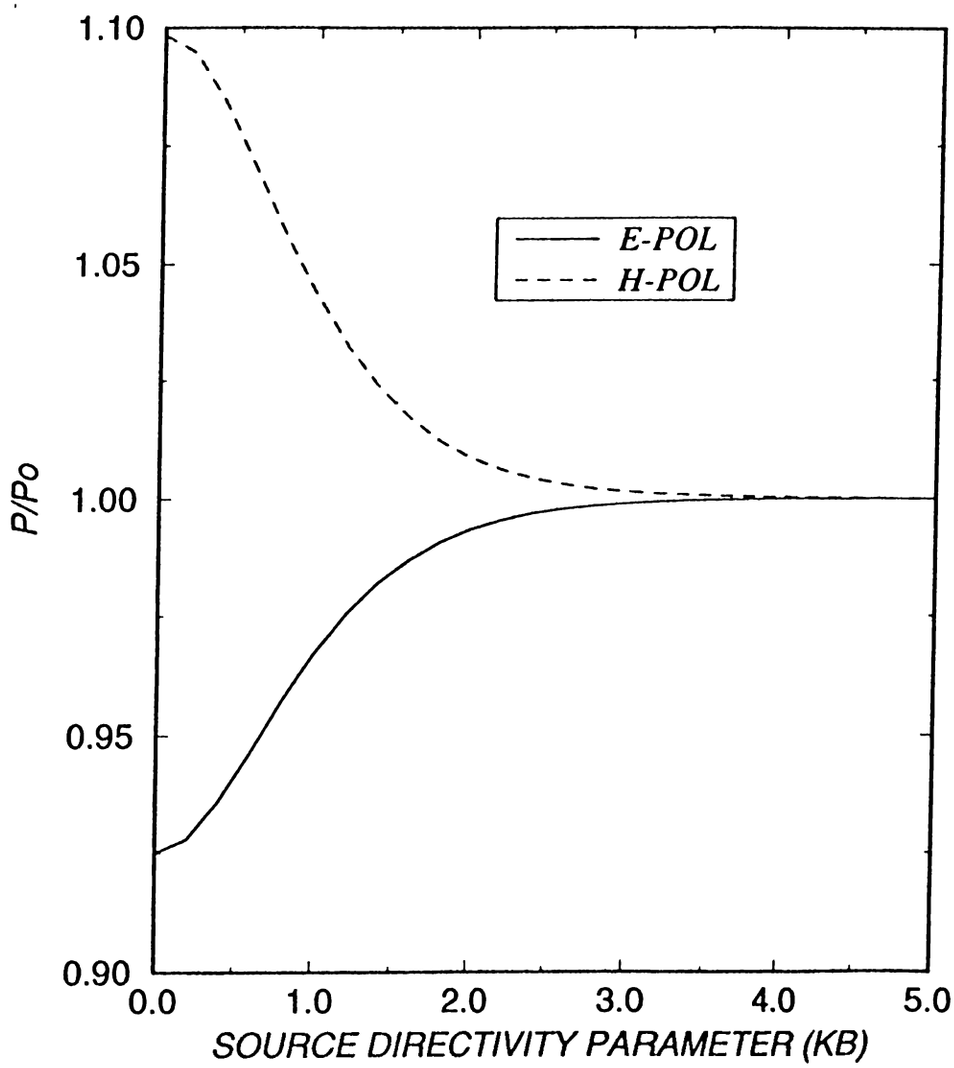

Figure 6.18: Total radiated power variation with increasing feed directivity parameter kb, for $\theta_{ap} = 15°$ and ka=50 (D=3.9λ).

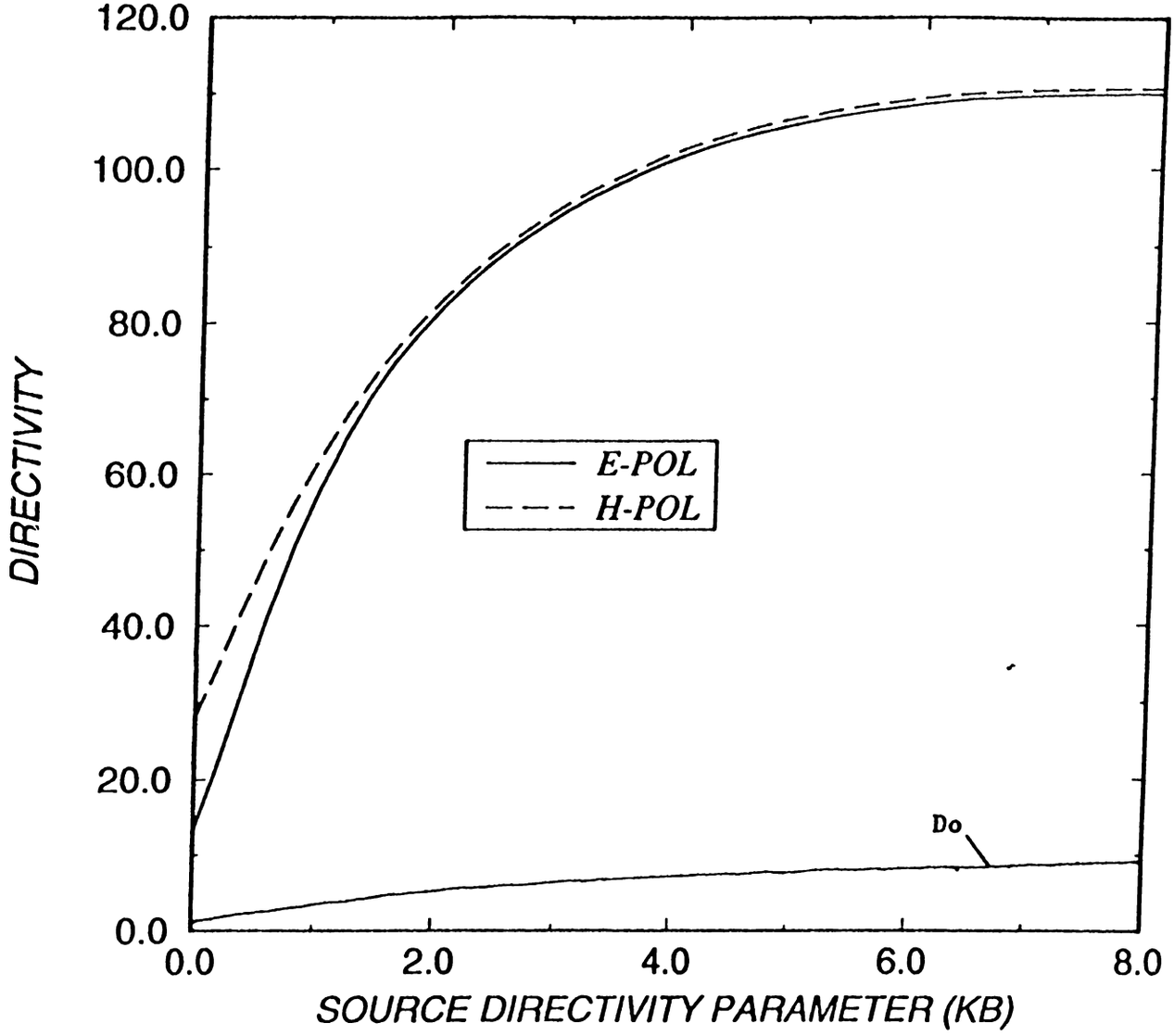

Figure 6.19: Directivity variation with increasing feed directivity parameter kb, for $\theta_{ap} = 30°$ and ka=62.8 (D=10λ).

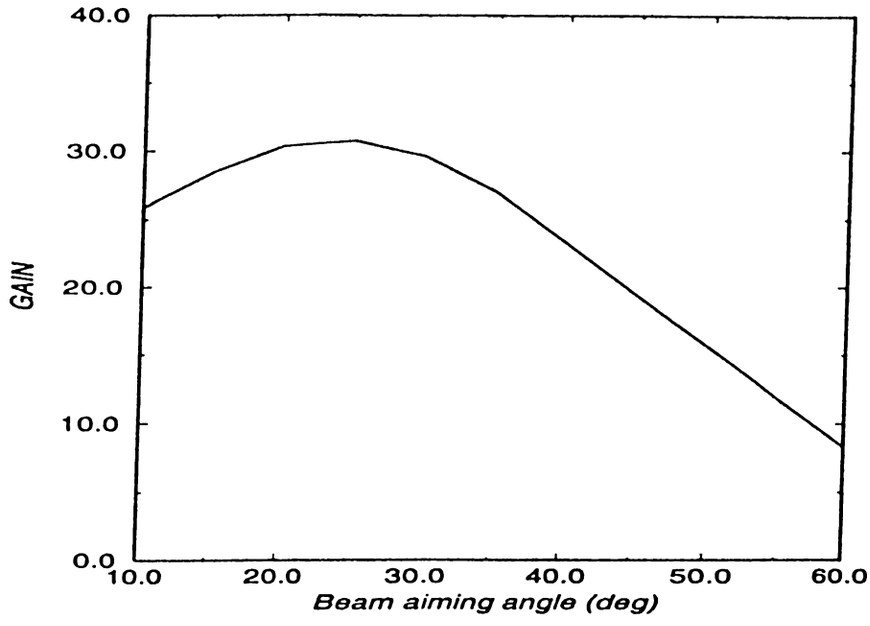

Figure 6.20: Variation of the directive gain with the beam aiming angle for the circular offset reflector of $F/D_P = 0.3$, h/D=0.125 and $D = 50\lambda$ where $\theta_{ap} = 25.56°$ and $\theta_o = 30.87°$.

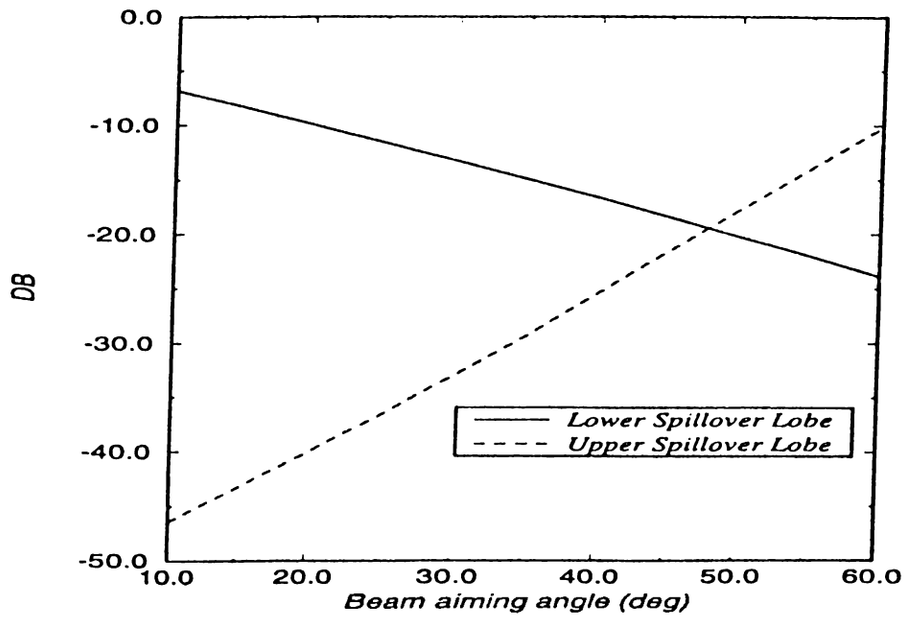

Figure 6.21: Variation of the spilloverlobe levels in dB with the beam aiming angle for the circular offset reflector of $F/D_P = 0.3$, h/D=0.125 and $D = 50\lambda$ where $\theta_{ap} = 25.56^o$ and $\theta_o = 30.87^o$.

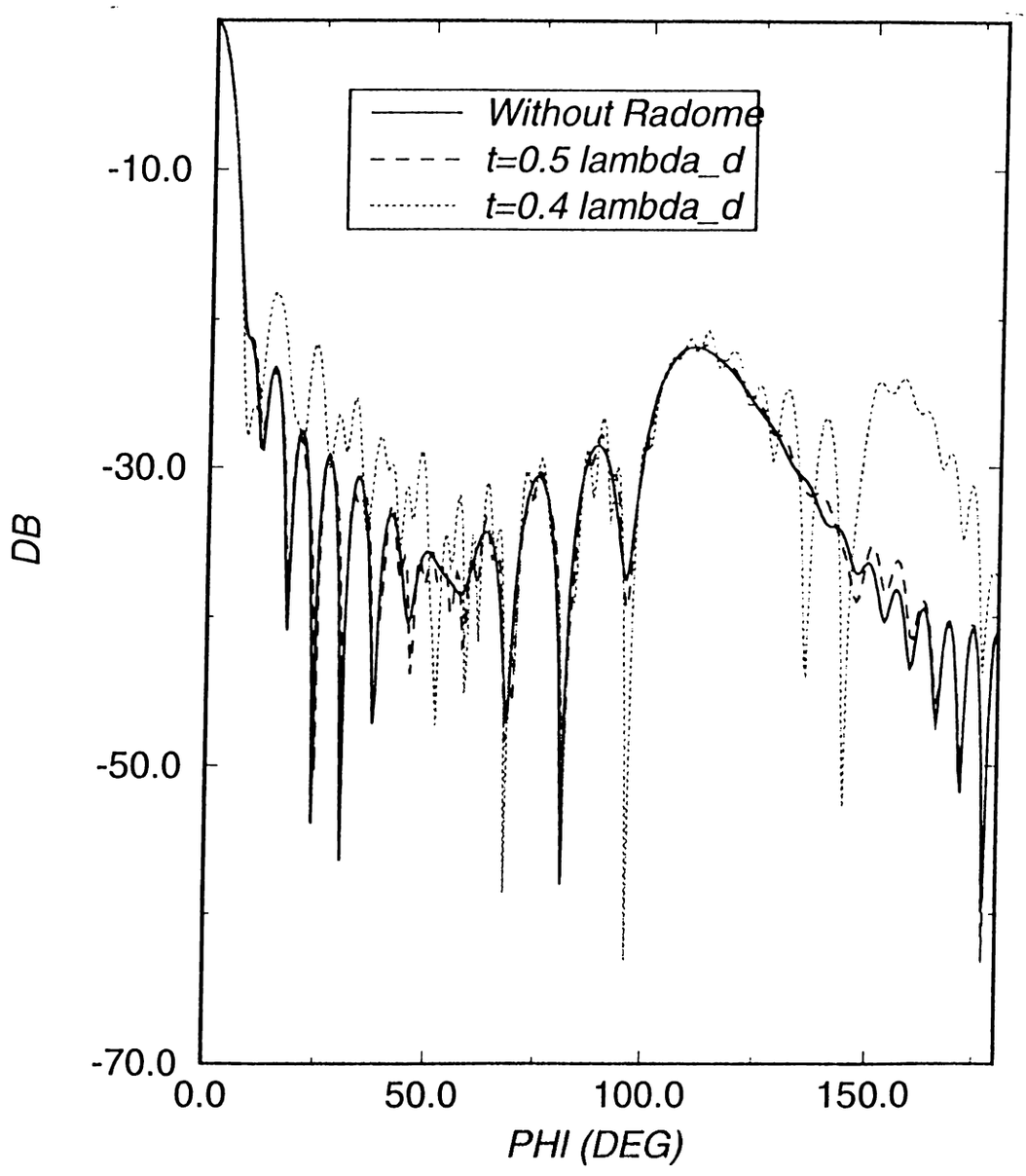

Figure 6.22: The radome effect on the radiation pattern for E-Polarization case. The radome geometry is defined as $ka = 62.8$, $kc = 78.5$ and $t = 0.5\lambda_d$. The permitivity of dielectric shell is 2. Feed directivity parameter $kb = 2.6$ corresponds to a $-9.92\,dB$ edge illumination.

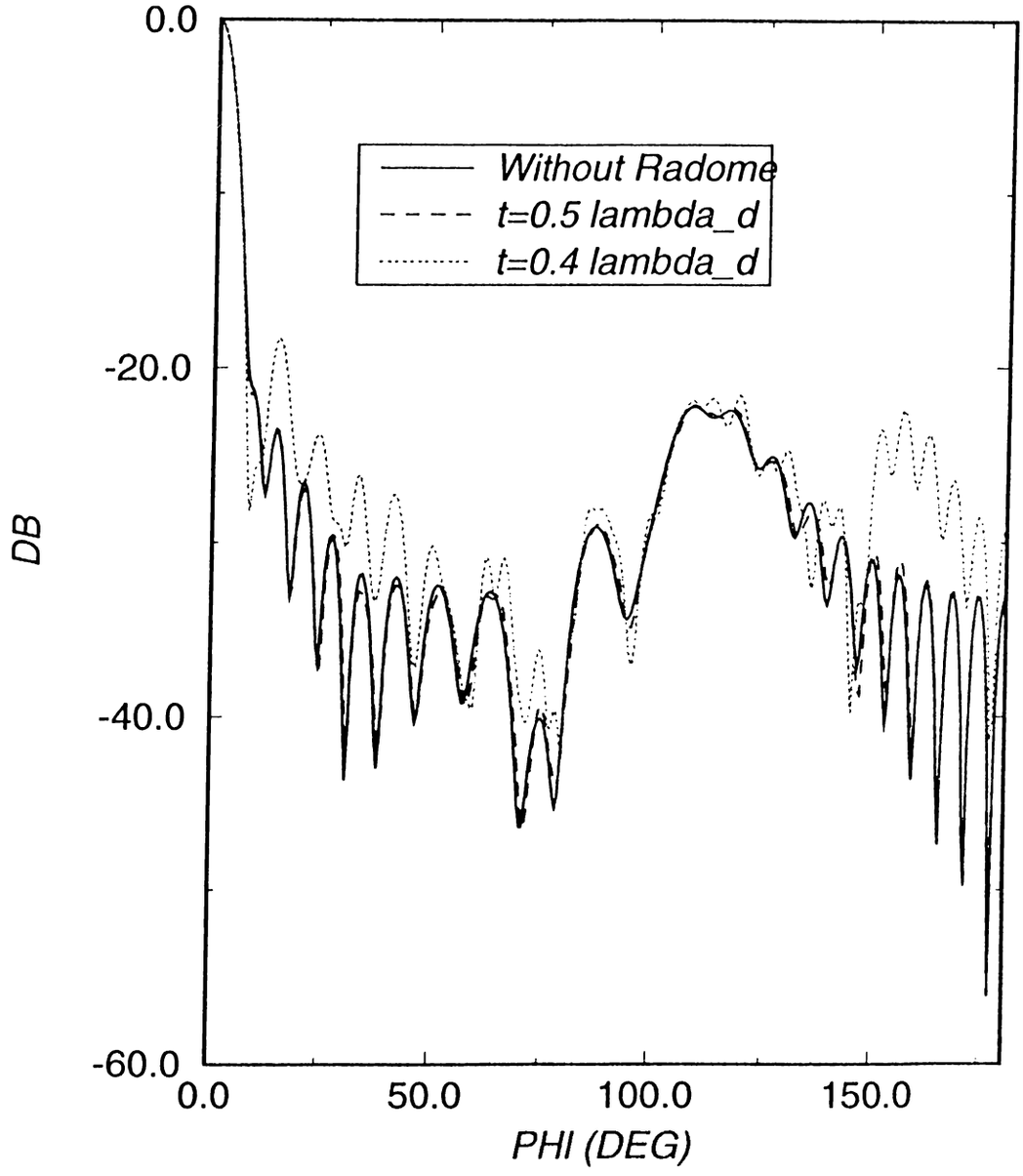

Figure 6.23: The radome effect on the radiation pattern for H-Polarization case. The radome geometry is defined as $ka = 62.8$, $kc = 78.5$ and $t = 0.5\lambda_d$. The permitivity of dielectric shell is 2. Feed directivity parameter $kb = 2.6$ corresponds to a $-9.92\,dB$ edge illumination.

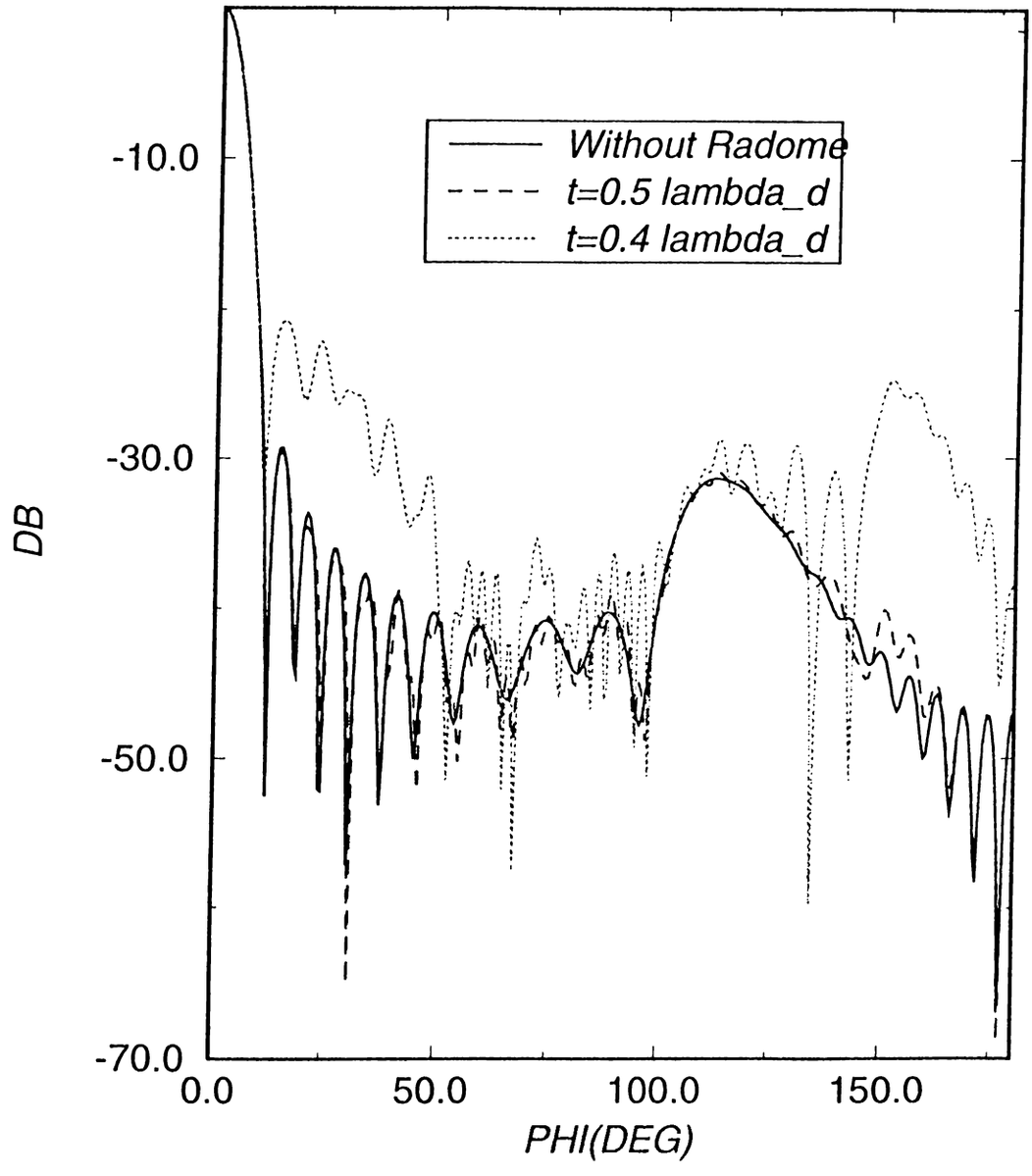

Figure 6.24: The radome effect on the radiation pattern for E-Polarization case. The radome geometry is defined as $ka = 62.8$, $kc = 78.5$ and $t = 0.5\lambda_d$. The permitivity of dielectric shell is 2. Feed directivity parameter $kb = 5$ corresponds to a $-18.21\,dB$ edge illumination.

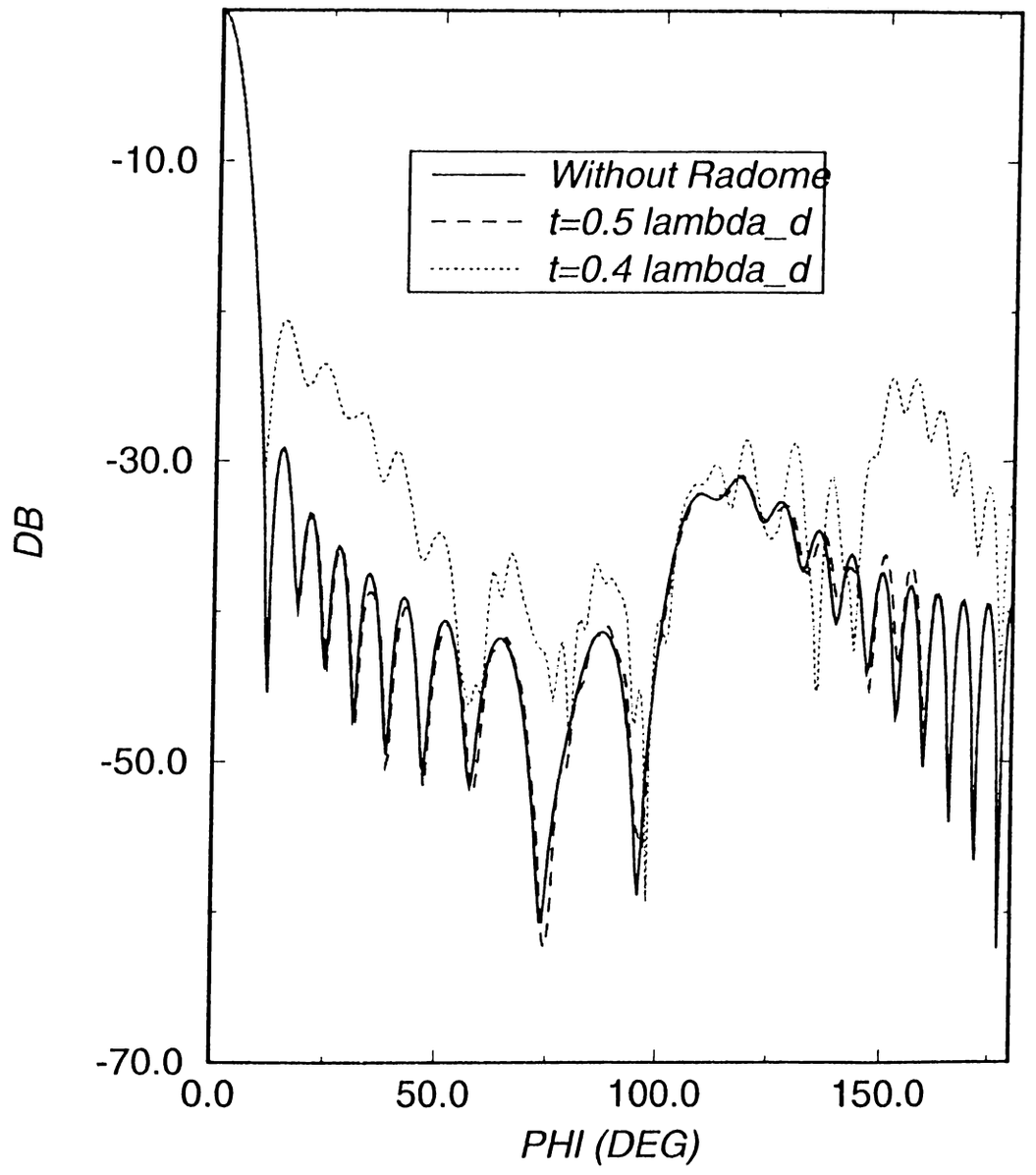

Figure 6.25: The radome effect on the radiation pattern for H-Polarization case. The radome geometry is defined as $ka = 62.8$, $kc = 78.5$ and $t = 0.5\lambda_d$. The permitivity of dielectric shell is 2. Feed directivity parameter $kb = 5$ corresponds to a $-18.21\,dB$ edge illumination.

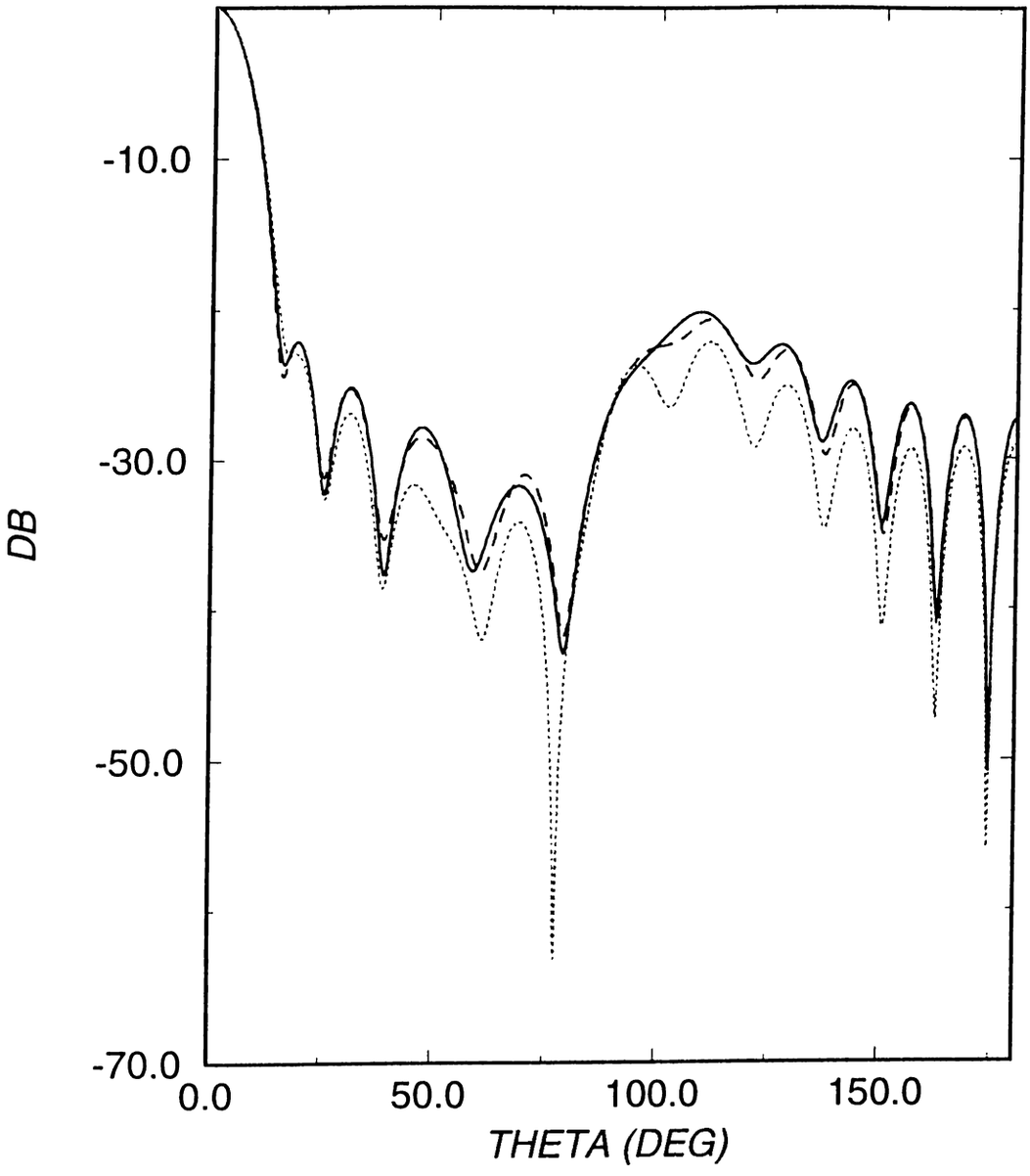

Figure 6.26: The radome effect on the radiation pattern for H-Polarization case. The radome is nonconcentrically located. The radome geometry is defined as $ka = 31.4$, $kc = 27.3$, $kL = 27.3$ and thickness of the radome is $t = 0.5\lambda_d$ (dashed curve) and $t = 0.4\lambda_d$ (dotted curve). The permitivity of dielectric shell is 2. Solid curve represents the reflector in free space. Feed directivity parameter $kb = 2.6$ corresponds to a $-9\,dB$ edge illumination.

Chapter 7

CONCLUSIONS

The Riemann-Hilbert Problem technique utilizing the idea of regularization is implemented to analyze a number of two-dimensional problems concerning electromagnetic wave scattering by cylindrically curved reflectors with or without dielectric radome covering.

By this approach, the dual series formulation arising due to the angular expansion of the relevant Green's function results in a well-conditioned matrix equation solved numerically. To simulate the feeder beam of the reflector antennas, the complex source point model is applied.

The reflector antennas in the free space and the similar antennas inside of a concentric or nonconcentric (shifted) dielectric radome cover are simulated. Both H and E polarization cases are considered assuming perfect electrical conductivity of the reflector. Far-field patterns, directivity and the total radiated power of the antennas are calculated for different values of the geometrical parameters of the reflector and the radome.

For the reflector inside of a concentric or nonconcentric radome, the effect of the radome on the antenna characteristics is analyzed.

By the present method, the principal results of the reflector antennas are verified and compared to the high-frequency approximate solutions available for 2-D parabolic reflectors. The advantages of the Riemann-Hilbert Problem technique as compared to the low-frequency Method of Moments or high-frequency Aperture Integration, Geometrical Theory of Diffraction and Physical Optics are demonstrated.

Since the approach is numerically rigorous within the adopted model, it can

be used to analyze the further properties of the reflector antennas accurately, such as the focal shift, front-to-back ratio and others.

The analysis can be extended to handle more complicated scatterers, for example, thin reflectors of non-zero resistivity and multilayer radomes of any permittivity and permeability.

Also, one can use the presented data as a benchmark to check the accuracy of the other numerical codes and approximate techniques.

Finally, it is worth mentioning that a similar approach can be used to simulate 3-D spherical reflectors, however the regularization procedure is based on another analytical technique[31,32].

Appendix A

Explicit expressions for some functions appearing in Chapter 4

The functions appearing in the solution for H and E-cases are as follows:

$$A^H_{mn} = \Delta^H_n(ka)T^H_{mn}, \quad A^E_{mn} = (-1)^{m+n}\Delta^E_n(ka)\frac{J_n(ka)H^{(1)'}_n(ka)}{J_m(ka)H^{(1)'}_m(ka)}T^E_{mn} \tag{A.1}$$

$$\Delta^H_n = |n| + i\pi(ka)^2 J'_n(ka)H^{(1)'}_n(ka), \qquad \Delta^E_n = |n| + i[\pi J_n(ka)H^{(1)}_n(ka)]^{-1}. \tag{A.2}$$

For $|n| > ka + 5$, both Δ^E_n and Δ^H_n go to zero as $O(|n|^{-1})$ with $|n| \to \infty$ [7]. Also,

$$T_{mn}(x) = \begin{cases} S_{mn}(x) & m \neq 0 \\ S_{n0}(x) & m = 0, n \neq 0 \\ -ln[(1+x)/2] & m = 0, n = 0 \end{cases} \tag{A.3}$$

where $S_{mn}(x)$ are defined via Legendre's polynomials $P_n(x)$ as

$$S_{mn}(x) = [2(m-n)]^{-1}[P_{m-1}(x)P_n(x) - P_m(x)P_{n-1}(x)] \tag{A.4}$$

If $n = m$, L'Hospital's rule reduces (26) to the following form

$$S_{mm}(x) = \frac{1}{2|m|}\sum_{s=0}^{|m|} U_{|m|-s}(x)P_{|m|-s-1}(x) \tag{A.5}$$

where $U_0(x) = 1, \quad U_1(x) = -x, ..., \quad U_n(x) = P_n(x) - 2xP_{n-1}(x) + P_{n-2}(x)$.

For $|n|, |m| \to \infty$ all the functions T_{mn} decay as $O(|m-n+1|^{-1}|mn|^{-\frac{1}{2}})$ uniformly for any $\theta_{ap} \neq 0$ or π [7].

References

[1] G. A. Suedan and E. V. Jull, "Beam diffraction by a half-plane and a wide slit," *IEEE Trans. AP.,* vol.35, pp. 1077-1083, 1987.

[2] G. A. Suedan and E. V. Jull, "Beam diffraction by planar and parabolic reflectors," *IEEE Trans. AP.,* vol. 39, pp. 521-527, April 1991.

[3] L. B. Felsen, "Complex source point solutions of the field equations and their relation to the propagation and scattering of Gaussian beams," *in Symp. Math.,* vol.18 , pp. 39-56, New York: Academic Press, 1976.

[4] M. R. Barclay and W. V. T. Rusch, "Moment-method analysis of large, axially symmetric reflector antennas using entire domain functions," *IEEE Trans. AP.,* vol. 39, pp. 491-496, April 1991.

[5] Z. S. Agranovich, V. A. Marchenko and V. P. Shestopalov, "Diffraction of a plane electromagnetic wave from plane metallic lattices," *Soviet Physics-Technical Physics, Engl. transl.,* vol. 7, no. 4, pp. 277-286, 1963.

[6] R. W. Ziolkowski, "N-series problems and the coupling of electromagnetic waves to apertures: a Riemann-Hilbert approach," *SIAM J. Appl. Math.,* vol. 16, pp. 358-378, 1985.

[7] R. W. Ziolkowski, "Scattering from cavity-backed apertures: The generalized dual series solution of the concentrically loaded E-Pol slit cylinder problem," *IEEE Trans. AP.,* vol. 35, no. 5, pp. 504-528, May 1987.

[8] A. I. Nosich, "Green's function - dual series approach in wave scattering by combined resonant scatterers," in M. Hashimoto, M. Idemen and O. A. Tretyakov (eds.), *Analytical and Numerical Methods in EM Wave Theory,* Tokyo: Science House, pp. 419-469, 1993.

[9] I. V. Lindell, "Methods for Electromagnetic Field Analysis," Oxford: Clarendon Press, 1992.

[10] V.I. Dmitriev and Y. V. Zakharov, "Integral Equations in Electromagnetic Boundary Value Problems," Moscow: Moscow University Press, 1987 (in Russian).

[11] Y. V. Zakharov and Y. V. Pimenov, "Numerical Methods in Radio Wave Diffraction," Moscow: Radio i Svyaz, 1982 (in Russian).

[12] W. L. Stutzman and G. A. Thiele, "Antenna Theory and Design," NY: Wiley, 1981.

[13] J. D. Kraus, "Antennas," McGraw-Hill, 1988.

[14] T. Lee, R. C. Rudduck and M. C. Bailey, "A surface distortion analysis applied to the hoop/column deployable mesh reflector antenna," *IEEE Trans. AP.,* vol. 37, pp. 452-459, April 1989.

[15] H. A. Kalhor, "Electromagnetic scattering by a dielectric slab loaded with a periodic array of strips over a ground plane," *IEEE Trans. AP.,* vol. 36, pp. 147-151, January 1988.

[16] J. J. Dongarra, "Performance of various computers using standard linear equations software," *Supercomputing Review,* pp. 73-80, January 1990.

[17] N. R. Kilcoyne, "A two dimensional ray-tracing method for the calculation of radome boresight error and antenna patern distortion," *Electro Science Lab., Ohio State Univ. Res. Foundation Rep.,* Rep no: 2767-2, oct. 2, 1969.

[18] D. C. F Wu and R. C. Rudduck, "Plane wave spectrum - surface integration technique for radome analysis," *IEEE Trans. AP.,* pp. 497-500, May 1974.

[19] P. D. Einziger and L. B. Felsen, "Ray analysis of two-dimensional radomes," *IEEE Trans. AP.,* vol. 31, no. 6, November 1983.

[20] X. J. Gao and L. B. Felsen, "Complex ray analysis of beam transmission through two-dimensional radomes," *IEEE Trans. AP.,* vol. 33, no. 9, September 1985.

[21] Ercument Arvas and Saila Ponnopalli, "Scattering cross section of a small radome of arbitrary shape," *IEEE Trans. AP.,* vol. 37, no. 5, May 1989.

[22] T. Oğuzer, A. Altıntaş and A. I. Nosich, "Analysis of circular reflectors by complex source-dual series approach," *IEEE AP-S Int. Symp. Digest, Ann Arbor,* pp. 922-925, June 1993.

[23] T. Oğuzer, A. Altıntaş and A. I. Nosich, "Accurate simulation of circular reflectors by the complex source-dual series approach," *Proc. ICEAA-93, Torino,* pp. 335-338, September 1993.

[24] A. I. Nosich, A. Altıntaş and T. Oğuzer, "Simulating millimeter reflector antennas," *Proc. SPIE-94, Int. Conf. on Millimeter and Submillimeter Waves and Applications,*

[25] T. Oğuzer, A. Altıntaş and A. I. Nosich, "Analysis of radome covered circular reflectors by complex source-dual series approach," *IEEE AP-S Int. Symp. Digest, Seattle,* pp. 70-73, June 1994.

[26] T. Oğuzer, A. Altıntaş and A. I. Nosich, "Accurate simulation of reflector antennas by complex source-dual series approach," *IEEE Trans. AP.,* vol. 43, no. 8, pp. 793-802, August 1995.

[27] W. Stutzman and M. Terada, "Design of offset parabolic reflector antennas for low cross-pol and low sidelobes," *AP Magazine,* vol. 35, pp. 46-49, December 1993.

[28] K. Pontoppidan, "Technical description of GRASP-7 and GRASPC," *TICRA Corp. Report,* S-359-03, Copenhagen, 1989.

[29] H. Ling, S. W. Lee, P. T. C. Lam and W. V. T. Rusch, "Focal shifts in parabolic reflectors," *IEEE Trans. AP.,* vol. 33, pp. 744-748, July 1985.

[30] M. S. Narasimhan and K. R. Govind, "Front-to-back ratio of of paraboloidal reflectors," *IEEE Trans. AP.,* vol. 39, pp. 877-882, July 1991.

[31] S. S. Vinogradov, "Reflectivity of a spherical shield," *Radiophysics Quantum Electronics, Engl. transl.,* vol. 26, no. 1, pp. 78-88, 1983.

[32] R. W. Ziolkowski and W. A. Johnson, "Electromagnetic scattering of an arbitrary plane wave from a spherical shell with a circular aperture," *J. Math. Physics,* vol. 28, no. 6, pp. 1293-1314, 1987.

[33] J. A. Roumeliotis and N. B. Kakogiannos, "Scattering from an infinite cylinder of small radius embedded into a dielectric one," *IEEE Trans. AP.,* vol. 42, no. 3, pp. 463-470, March 1994.